GEODYNAMICS & TECTONOPHYSICS
Published by the Institute of the Earth's Crust, Siberian Branch, Russian Academy of Sciences

TECTONOPHYSICS

2022 VOLUME 13 ISSUE 3 ARTICLE 0646

ISSN 2078-502X

DOI: 10.5800/GT-2022-13-3-0646

GEOLOGICAL FEATURES IDENTIFIED FROM FIELD OBSERVATIONS AND REMOTE SENSING DATA ON THE UM TAGHIR AREA, EASTERN DESERT, EGYPT

H.A. Awad [1,2], **I.A. El-Leil** [3], **M. Kamel** [2], **A. Tolba** [2], **A.V. Nastavkin** [1], **R.M. El-Wardany** [2,4]

[1] Southern Federal University, 40 Zorge St, Rostov-on-Don 344103, Russia
[2] Assuit Branch of the Al-Azhar University, Assuit 71524, Egypt
[3] Al-Azhar University, Cairo, Egypt
[4] School of Earth Science and Resources of the Chang'an University, Xi'an 710064, China

ABSTRACT. The current study presents the integration between field observations and remotely sensed data for detection and extraction of geological structural features using Sentinel-2A and Aster DEM images. The area under investigation is represented by the Neoproterozoic East African Orogeny encompassing a part of the Arabian Nubian Shield. All the rock units studied belong to the Late Cryogenian-Ediacaran periods that are divided into two large terrains (continental arc terrain and oceanic arc terrain). The metagabbro and metavolcaniclastic rocks make up the oceanic terrain, while the gabbro, tonalite, granodiorite, dokhan volcanic, monzogranite and alkali feldspar granite comprise continental arc terrain. The Sentinel-2A remote sensing and ASTER DEM data have meaningful application in respect of geological interpretation. Lineament analysis is one of the most useful tools in geological mapping and mineral exploration. Several methods of processing and extracting lithological information and lineaments were applied to the Sentinel-2A and ASTER DEM data covering the present study. The methods include various image enhancements (FCC, MNF and PCA) and the application of directional filters (Sobel). The study results show that the area was subjected to stresses of various directions (WNW – ESE, NW-SE, NE-SW, N-S, NNE – SSW, and E-W). There occurred some important structure-related and mineralization events like migmatization (in granodiorites) and bearing mineralization (in gabbro), which are associated with major elements of evidence-based structural control of the area and with the proximity of the Quena Safaga shear zone-related mineralization.

KEYWORDS: ASTER DEM; lineaments extraction; Sentinel-2A; Um Taghir; Egypt

FUNDING: The researcher (H.A.M. Awad) is funded by a scholarship under the Joint Executive Program between Egypt and Russian Federation.

RESEARCH ARTICLE

Received: March 1, 2021
Revised: March 9, 2022
Accepted: March 15, 2022

Correspondence: Hamdy A. Awad, hamdiawaad@gmail.com

FOR CITATION: Awad H.A., El-Leil I. A., Kamel M., Tolba A., Nastavkin A.V., El-Wardany R.M., 2022. Geological Features Identified from Field Observations and Remote Sensing Data on the Um Taghir Area, Eastern Desert, Egypt. Geodynamics & Tectonophysics 13 (3), 0646. doi:10.5800/GT-2022-13-3-0646

ГЕОЛОГИЧЕСКИЕ ПРИЗНАКИ, ВЫЯВЛЕННЫЕ ПО ДАННЫМ ПОЛЕВЫХ НАБЛЮДЕНИЙ И ДИСТАНЦИОННОГО ЗОНДИРОВАНИЯ В РАЙОНЕ УМ ТАГИР, ВОСТОЧНАЯ ПУСТЫНЯ, ЕГИПЕТ

Х.А. Авад[1,2], И.А. Эль-Лейл[3], М. Камель[2], А. Толба[2], А.В. Наставкин[1], Р.М. Эль Вардани[2,4]

[1] Южный федеральный университет, 344103, Ростов-на-Дону, ул. Зорге, 40, Россия
[2] Университет аль-Азхар, Асьютский филиал, 71524, Асьют, Египет
[3] Университет аль-Азхар, Каир, Египет
[4] Школа наук о Земле и природных ресурсах Чанъаньского университета, 710064, Сиан, Китай

АННОТАЦИЯ. Темой исследования является интеграция данных полевых наблюдений и дистанционного зондирования с целью обнаружения и извлечения геолого-структурных признаков с помощью спутниковых снимков Sentinel-2A и цифровой модели рельефа ASTER DEM. Исследуемый район представляет собой неопротерозойскую восточно-африканскую орогению, охватывающую часть Нубийско-Аравийского щита. Изучаемые толщи пород относятся к позднему криогению – эдиакарию и образуют два террейна (континентальный дуговой террейн и океанический дуговой террейн). Океанический террейн сложен метагаббро и метавулканокластическими породами, а габбро, тоналиты, гранодиориты, доханские вулканиты, монцониты и щелочные полевошпатовые граниты слагают континентальный дуговой террейн. Данные со спутника Sentinel-2A, а также данные ASTER DEM используются для геологической интерпретации. Линеаментный анализ является одним из наиболее полезных инструментов геологического картирования и разведки полезных ископаемых. В рамках исследования были использованы методы для обработки данных Sentinel-2A и ASTER DEM, извлечения литологической информации из снимков и проведения линеаментного анализа снимков. Это различные методы увеличения изображения (FCC, MNF и PCA) и применения направленных фильтров (Sobel). Результаты исследования указывают на то, что в данной области имели место напряжения различной направленности (ЗСЗ – ВЮВ, СЗ-ЮВ, СВ-ЮЗ, С-Ю, ССВ – ЮЮЗ и В-З). Образовалось несколько крупных сопутствующих структур и произошло несколько событий в процессе минерализации, таких как мигматизация (в гранодиоритах) и минерализация по простиранию (в габбро), обусловленных главными элементами научно обоснованного структурного контроля территории и близостью нахождения минерализованной зоны сдвига Кена-Сафага.

КЛЮЧЕВЫЕ СЛОВА: ASTER DEM; извлечение линеаментов; Sentinel-2A; Ум Тагир; Египет

ФИНАНСИРОВАНИЕ: Работа выполнена в рамках Программы сотрудничества между Египтом и Российской Федерацией.

1. INTRODUCTION

The Um Taghir area is one of the Neoproterozoic components of the North Arabian–Nubian Shield that was constrained to the East African Orogen (EAO) during the consolidation of Gondwana through the accretion of plateaus [Stern, 1994; Kröner et al., 1994; Abdelsalam, Stern, 1996]. A detailed description is provided about three key orogenies that eventually shaped the formation of Greater Gondwana. The EAO resulted from the collision of the Arabian – Nubian Shield (ANS) and amalgamated arc terrains with the Sahara and Congo–Tanzania cratons to the west, as well as with Amazonia and Afif terrains to the east, which gave rise to the formation of major continental blocks between the Congo–Tanzania – Bangwenla Craton and the Indian Shield [Collins, Pisarevsky, 2005]. The ANS is about 3500 km in length and about 1500 km in width, thereby representing the world's biggest span of mantle-derived, juvenile Neoproterozoic crust, whereas the EAO is just around 2.7×106 km^2 [Johnson et al., 2011]. The studied area belongs to the rock units cropping out in the far north-western section of the ANS and is assigned the late Cryogenian-Ediacaran age (690–600 Ma) [Johnson et al., 2011]. In the northern part of the ANS, there occur the protoliths that are assigned the middle-late Cryogenian age (780–680 Ma). In this study, the field research was conducted in the area that is influenced by the Qena-Safaga Shear zone, the Egypt's largest fault shear zone in the central Eastern Desert [El-Gaby et al., 1988]. This shear zone has caused the formation of both metamorphic and non-metamorphic magmatic rocks in the study area, thereby dividing the studied rock units into two major terrains – oceanic magmatic arc terrain (metavolcaniclastic sequences and metagabbro) and continental magmatic arc terrains (metavolcaniclastic sequences and metagabbro) (late-to-post-orogenic magmatism). The low-grade metamorphic rocks of the oceanic terrains along the Qena-Safaga Shear Zone represent a part of the old upper crust, that thrusts over the young lower crust composed of high-grade metamorphic rocks (gneisses and migmatites) [El-Leil et al., 2015]. Undoubtedly, the remote sensing data application has brought new opportunities for the lithological identification and structural mapping. Several spatial and spectral resolutions of remote sensing data provide global coverage of the Earth's surface [Soulaimani et al., 2014; Dos Reis Salles et al., 2017]. This can provide detailed information on surface features at different levels. The most important features of the surface are the linear features and the rock units [Pirasteh et al., 2013]. The study of the concept of lineament extraction from digital satellite images has been aimed at conducting structural and tectonic analysis [Madani, 2001; Sedrette, Rebai, 2016; Si Mhamdi et al., 2017] and mineral exploration [Mars, Rowan, 2006; Farahbakhsh et al., 2018].

In general, there are distinguished two types of linear features man-made/artificial (e.g. roads, railroads, etc.) and natural ones (e.g. geological lineaments, drainage networks, etc.). These features are easily detected/detectable by remote sensing data processing techniques. Determining linear features in remote sensing images can be complicated because their spatial and spectral characteristics vary across the extensions [Wang, Howarth, 1993]. There are several techniques to derive some linear features from digital satellite data for various applications, particularly for the road network determination [Valero et al., 2010]. Lineament identification and extraction in remote sensing can be carried out through two approaches including manual extraction, which mainly depends on visual interpretation and general knowledge of an interpreter [Ramli et al., 2010], and automatic lineament extraction using computer software and algorithms [Morris, 1991; Prasad et al., 2013]. Several studies have been carried out to extract lineaments automatically using computer algorithms. Many researchers used LINE module of PCI Geomatica [Kocal et al., 2004; Adiri et al., 2017; Javhar et al., 2019].

Analysis and interpretation of the aeromagnetic and remote sensing data allowed mapping the subsurface and surface extension of geologic structures [Abuelnaga et al., 2019; Eldosouky, 2019; Sehsah, Eldosouky, 2020; Eldosouky, Saada, 2020; Pham et al., 2020, 2021; Eldosouky, Mohamed, 2021].

The remote sensing helped several researchers to carry out geological mapping and Earth exploration [Sulaksana, Helman, 2014; Abdullah et al., 2013; Papadaki et al., 2011]. The structural geology features, and economic and environmental-geologic behavior were detected based on the fault as one of the most important geologic structures in the fieldwork study [Colwell et al., 1983; Drury, 1987].

In the last decade, the use of remote sensing applications in lithological and structural mapping was more effective. Based on the previous studies and pre-drawn geological maps, as well as on the Enhanced Thematic Mapper Plus (ETM+), ASTER DEM and Sentinel-2A, the remote sensing data are used to make an initial geological interpretation. Sentinel-2A is the most advanced satellite with data freely available for long range and high frequency remote sensing applications. Sentinel-2A data is one of the effective tools for remote sensing applications [Mandanici, Bitelli, 2016]. The Sentinel-2A remote sensing data provides more detail on the NIR and SWIR ranges, which can be applied successfully in different contexts including geological mapping, agriculture monitoring, and natural disaster management The Sentinel-2A data is being used for applications like-rock study, structural mapping, and mineral exploration [Van der Meer et al., 2014; El Kati et al., 2018; Li et al., 2018]. Some authors have conducted many studies on structural lineament length and density [Casas et al., 2000; Koike et al., 1995; Ni et al., 2016; Liu et al., 2021]. These studies applied advanced technology and computer programs to compute and analyze the length and density data. The Sentinel-2A data processing analysis involves the relationship between spectral absorption/emission and mineralogical compositions of rock units to characterize the rocks under investigation. Here we present the preliminary results of the study aimed to apply the Sentinel-A2 remote sensing and ASTER DEM data to identify structural features and to construct a new geological map of the study area. The Um Taghir area is located west of Safaga City at the extreme northern boundary of the Central Eastern Desert of Egypt (Fig. 1). Its area is about 900 km^2, between longitudes 33°35'00" and 33°50'00" and latitudes 26°35'00" and 26°49'00".

2. MATERIAL AND METHODS

This study was based on the data set of Sentinel-2A remote sensing and ASTER DEM data. We aimed to discriminate between lithological units and structural lineaments and collect field evidence related.

There have been several data sources and materials used in this work. The remote sensing dataset collected includes the Sentinel-2A and ASTER DEM data used for lithological identification and structural lineament extraction with field validation. Based on ASTER DEM, the study area is characterized by low to relatively high topography reliefs varying from 599 to 1032 m above the sea level (Fig. 2, a), as well as it is displayed on the previous geologic map (Basement rock of Safajah Quadrangle map 1:100000 of the Egyptian Geological Surveying and Mining Authority [Boulos et al., 1987] (Fig. 2, b).

The extraction of lineaments includes several steps: 1) pre-processing of remote sensing data (correction) using specific software programs (Envi 5.1, Erdas 2014 and QGIS), 2) processing of remote sensing data by PCI Geomatica 16 software to extract the lineament features from the raster data (Sentinel-2A and ASTER DEM data). A new layer must be corrected by removing and filtering irrelevant structures with knowledge-based ArcGIS v10.2.2 software. After that, the resultant structural lineaments were subjected to geometric calculation to obtain polyline angles using Rockworks 17 software to create a rose diagram. The rose diagram shows lineament directions. There have been produced structural lineament density maps.

Sentinel-2A Multi-Spectral Instrument (MSI) is the result of cooperation between the European Space Agency (ESA) and the U.S. Geological Survey (USGS). It is a part of a larger set of ESA missions focusing on different aspects of the Earth observation. The first Sentinel-2A satellite was launched on June 23, 2015 at 01:52 UTC on a Vega launch vehicle. It has an orbital swarth width of 290 km, ID, S2A_MSIL1C_20180824T081601_N0206_R121_T36RWQ_20180824T103944.SAFE, and a sun-synchronous polar orbit with a 10-day cycle. The Sentinel-2 satellite pair has an altitude of 786 km and provides the 5-day repeat coverage. The Sentinel-2A multi-Spectral In-strument (MSI)

Fig. 1. Sentinal-2A (4, 2 and 1) image showing the location of the study area.
Рис. 1. Снимок изучаемой территории со спутника Sentinel-2A (4, 2 и 1).

Table 1. Sentinel-2A bands
Таблица 1. Полосы захвата Sentinel-2A

Sentinel-2A bands	Central wavelength (nm)	Bandwidth (nm)	Spatial resolution (m)
Band 1 – Coastal aerosol	442.7	21	60
Band 2 – Blue	492.4	66	10
Band 3 – Green	559.8	36	10
Band 4 – Red	664.6	31	10
Band 5 – Vegetation red edge	704.1	15	20
Band 6 – Vegetation red edge	740.5	15	20
Band 7 – Vegetation red edge	782.8	20	20
Band 8 – NIR	832.8	106	10
Band 8A – Narrow NIR	864.7	21	20
Band 9 – Water vapour	945.1	20	60
Band 10 – SWIR – Cirrus	1373.5	31	60
Band 11 – SWIR	1613.7	91	20
Band 12 – SWIR	2202.4	175	20

data on the current study has been downloaded for free from the European Space Agency website (https://scihub.copernicus.eu/dhus/). There are 13 Sentinel-2A bands that cover the visible to near-infrared spectral ranges (Table 1). The current Sentinel-2A remotely sensed data was acquired on August 24, 2018. The ASTER DEM 30 m spatial resolution data is used to facilitate the lineaments extraction of the current study. DEM provides a visual perspective and eliminates the problem associated with the lack of the coverage of the stereo mapping images.

Several Digital Image Processing (DIP) techniques have proven useful in enchancing the lineaments on satellite images with false-color composite, principal component analysis (PCA), band ratio, and edge enhancement filters. The Sentinel-2A (10 m) remote sensing data was used to enhance the surface features. The ASTER DEMs were also used to identify the lineament features.

Eight separate shaded relief images with light sources coming from eight different directions have been derived based on ASTER DEM to detect the Um Taghir area's lineament features. Each one has a different solar azimuth (sun angle), but the solar elevation and ambient light setting are 45° and 0.20, respectively, for all eight shaded relief images.

The other seven shaded images were derived from seven contrasting illumination directions 45°, 90°, 135°, 180°, 225°, 270°, and 315°. There was used the automatic method of line extraction from the shaded relief images. Any linear features, especially structural lineaments, are characterized by change of tone as compared with the surrounding features. Edge enhancement is an effective technique to enhance these features. This technique was applied to all shaded relief images before lineaments extraction process to increase image clarity and contrast.

To complete the lineament extraction process using PCI, Geomatica software must run a set of procedures and steps. These steps were performed based on all the features extracted from shaded relief ASTER DEM images with the following software specific parameters (Table 2).

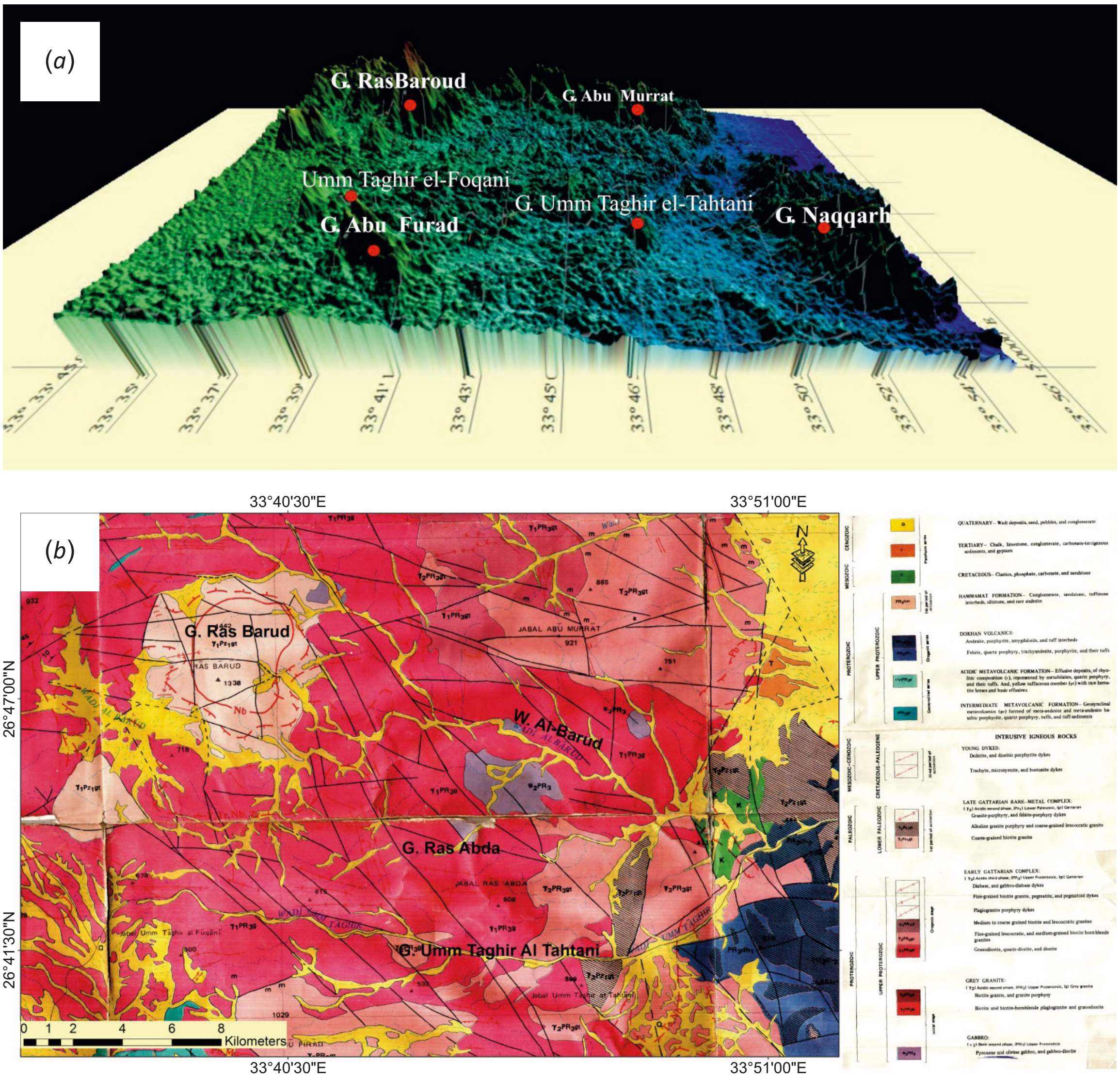

Fig. 2. Aster DEM image showing the topography (*a*), geologic map (after [Boulos et al., 1987]) of the study area (*b*).

Рис. 2. Цифровая модель рельефа ASTER DEM изучаемой территории (*a*), геологическая карта (по [Boulos et al., 1987]) (*b*).

The Sentinel-2A satellite remote sensing data was used herein to detect and identify the lithological units and lineament extraction features (faults, joints, and dikes) distributed throughout the study area.

The Minimum Noise Fraction (MNF), the False Color Composite (FCC), the Principal Components Analysis (PCA) and the Color Ratio Composite (CRC) enhancement techniques have been applied to Sentinel-2A images for their differentiation and contrast theme channel.

Two MNF (3, 2, 1) and (3, 4, 2) in the RGB images were selected to detect different rock units and linear features in the study area. The FCC (12, 8, 2) in the RGB was the most appropriate alternative to provide the ability to distinguish between different rocks, representing a larger number of different lineament features overdetermined in the study area. PCA from bands (5, 1, 2) and (4, 1, 5) were chosen to enhance lithological features and compared to band ratio combinations (2/7, 5/10, 8/2) and (3/7, 5/9, 6/10) to extract the lineament easily.

Table 2. Parameters used as input values for the automated feature extraction algorithm

Таблица 2. Параметры, используемые в качестве входных значений для алгоритма автоматического извлечения признаков

Name	Description	Values
RADI	Radius of filter in pixels	10
GTHR	Threshold for edge gradient 90	110
LTHR	Threshold for curve length 30	30
FTHR	Threshold for line fitting error	12
ATHR	Threshold for angular difference	30
DTHR	Threshold for linking distance 20	20

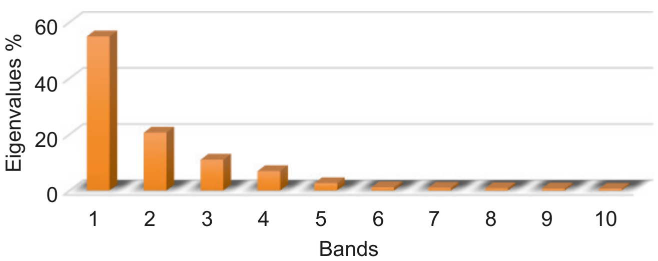

Fig. 3. Histogram shows Eigenvalues % of Sentinal-2A of the study area.

Рис. 3. Гистограмма собственных значений % Sentinel-2A изучаемой территории.

The minimum noise fraction (MNF) technique is applied to the remote sensing raw data to segregate noise in the data, and to shorten the set of subsequent computational requirements [Boardman et al., 1995]. Ten bands of Sentinel-2A data (Visible (2-3-4), VRE (5-6-7), NIR (8a-8) and SWIR (11-12)) were used in the minimum noise fraction techniques because they contain timely information to detect lithology of the rocks studied. The outcome results of the application of MNF on Sentinel-2A data showed an inverse relationship between the eigenvalues and noise (Table 3; Fig 3). MNF (3,2,1) was chosen as best because of its high-rate eigenvalues and less noise, and the ability to discriminate between the lithological units and detect the lineament features in these MNF combinations.

3. GEOLOGIC SETTING

The investigated rock units originate from the EAOs Late Cryogenian-Ediacaran magmatism as they are represented by the Island Arc assemblage (Oceanic crust terrain) and late-to-post-amalgamation (Continental crust terrain) [Johnson et al., 2011]. The metavolcaniclastic sequence and metagabbro of the island arc assemblage form the oceanic terrain, whereas the various magmatic rocks, such as gabbro, tonalite-granodiorite, dokhan volcanic, monzogranite, alkali feldspar granites and dikes represent the continental crust terrain as seen in Table 4 and Fig. 4 and Fig. 5.

4. REMOTE SENSING DATA ANALYSIS

Currently, the remotely sensed data is one of the most effective tools for geological mapping. The analysis of Sentinel-2A remotely sensed data can serve a basis for an easy and accurate identification of; lithological units and their boundaries in a study area.

4.1. Minimum Noise Fraction

The proposed Sentinel-2A MNF images (3, 2, 1) and (3, 4, 2) in the RGB are the best MNF false-color combinations used for geological discrimination of the study area.

The older rock unit (metavolcanoclstic) in the study area has a reddish blue color, while the metagabbro is characterized by a blue color. On the other hand, the gabbroic rock is shown having light blue color, and dokhan volcanic is characterized by a cyan color (Fig. 6). The granitoid rocks are differentiated into four types: tonalite (light pink), granodiorite (yellowish-brown), monzogranite (dark red) and alkali feldspars (red color). The basic dikes and the leucocratic granitic dikes have violet and pale pink colors, respectively, while wadi deposits appear to be green.

Table 3. Eigenvectors and eigenvalues (%) for the Sentinal-2A images of the study area

Таблица 3. Собственные векторы и собственные значения (%) для анализа изображений изучаемой территории со спутника Sentinel-2A

Bands	B2	B3	B4	B5	B7	B7	B8a	B8	B11	B12	Total
Eigenvector	139.47	52.33	27.82	17.51	6.52	2.78	2.36	1.98	1.75	1.48	254.03
Eigenvalues %	54.90	20.60	10.95	6.89	2.56	1.09	0.93	0.78	0.69	0.58	100 %

Table 4. Geochronology of the basement rocks in the study area
Таблица 4. Геохронология пород фундамента в пределах изучаемой территории

	Orogenic setting					Rock units	Age (Ma)	Reference (Age)
Late Cryogenian-Ediacaran magmatism	East African orogen EAO	Late-post amalgamation	Late to post-orogenic	Continental crust assemblage	Late to post-orogenic	Dikes Alkali-feldspar granite Monzogranite Dokhanvolcanic Tonalite- granodiorite Gabbro	650–542	[Johnson et al., 2011]
		Arc amalgamation	Early orogenic	Oceanic crust	Island arc assemblage	Metagabbro metavolcanoclastic	>650	

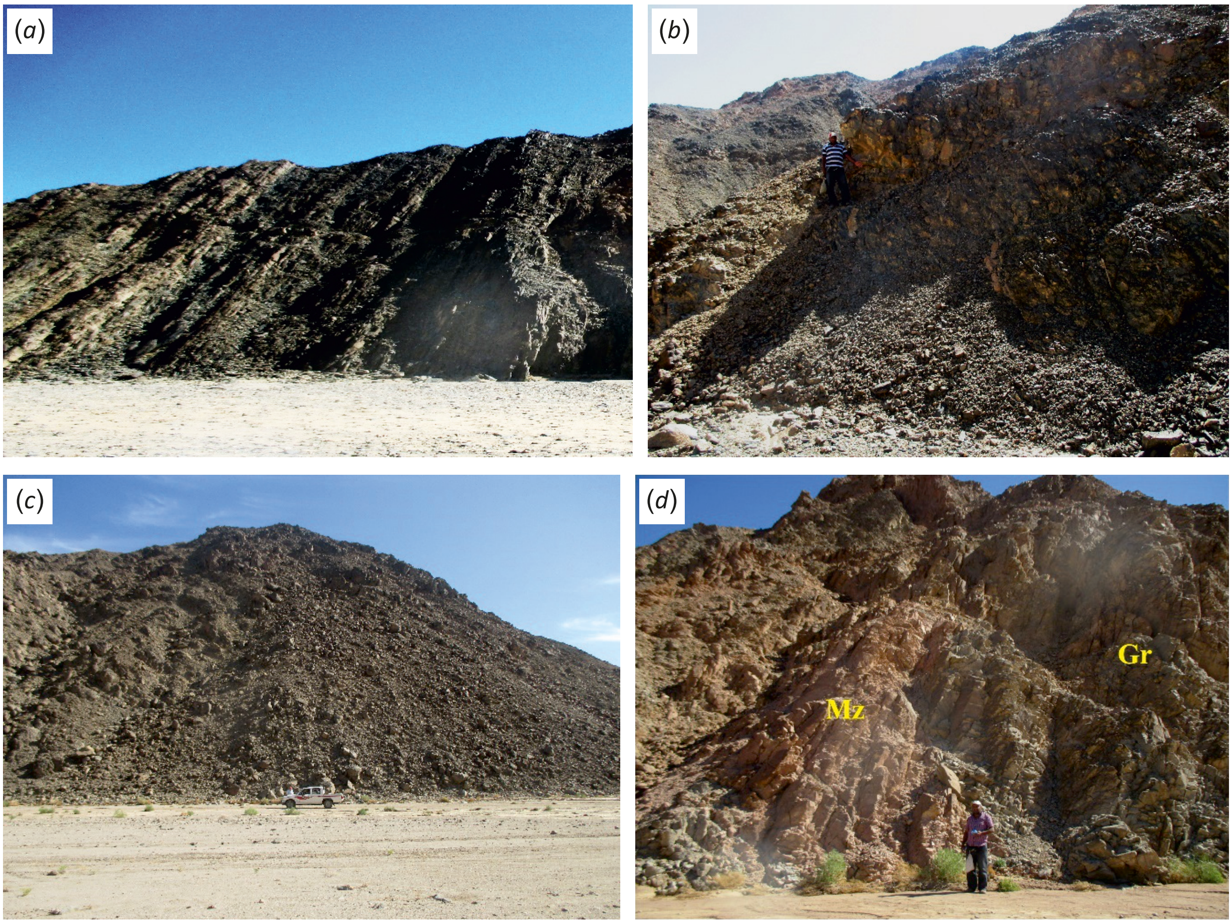

Fig. 4. Field photographs of schist (*a*), metagbbro (*b*), low hill of gabbro (*c*) and granodiorite (Gr) intruded by monzogranite (Mz) (*d*).
Рис. 4. Фотографии сланцев (*a*), метагаббро (*b*), низкогорья, сложенного породами габбрового состава (*c*) и гранодиоритов (Gr), интрудированных монцогранитами (Mz) (*d*), сделанные в полевых условиях.

Another best MNF composite image is (3, 4, 2) in the RGB (Fig. 7), with the lithological units easily discriminated. The metavolcanoclstic and metagabbro rocks are characterized by clearly defined brownish-green and green colors. The granitic rocks are differen-tiated into granodiorite (dark pink), monzogranite (yellowish green) and alkali granite (green color), wheres tonalite rock as well as the MNF (3, 4, 2) failed to be identifiedy tonalite rock. The gabbroic rock exhibits a light green color, while the dokhan volcanic is distinguishable by violet color. On the other hand, wadi deposits are characterized by a cyan color.

4.2. False Color Composite (FCC)

The False-color composite representation of the Sentinel-2A images shows differentiation between the rock units. In addition, it is used to detect the lineament features that are marked by contrast differences. The boundaries between geological units in the present study are better defined on

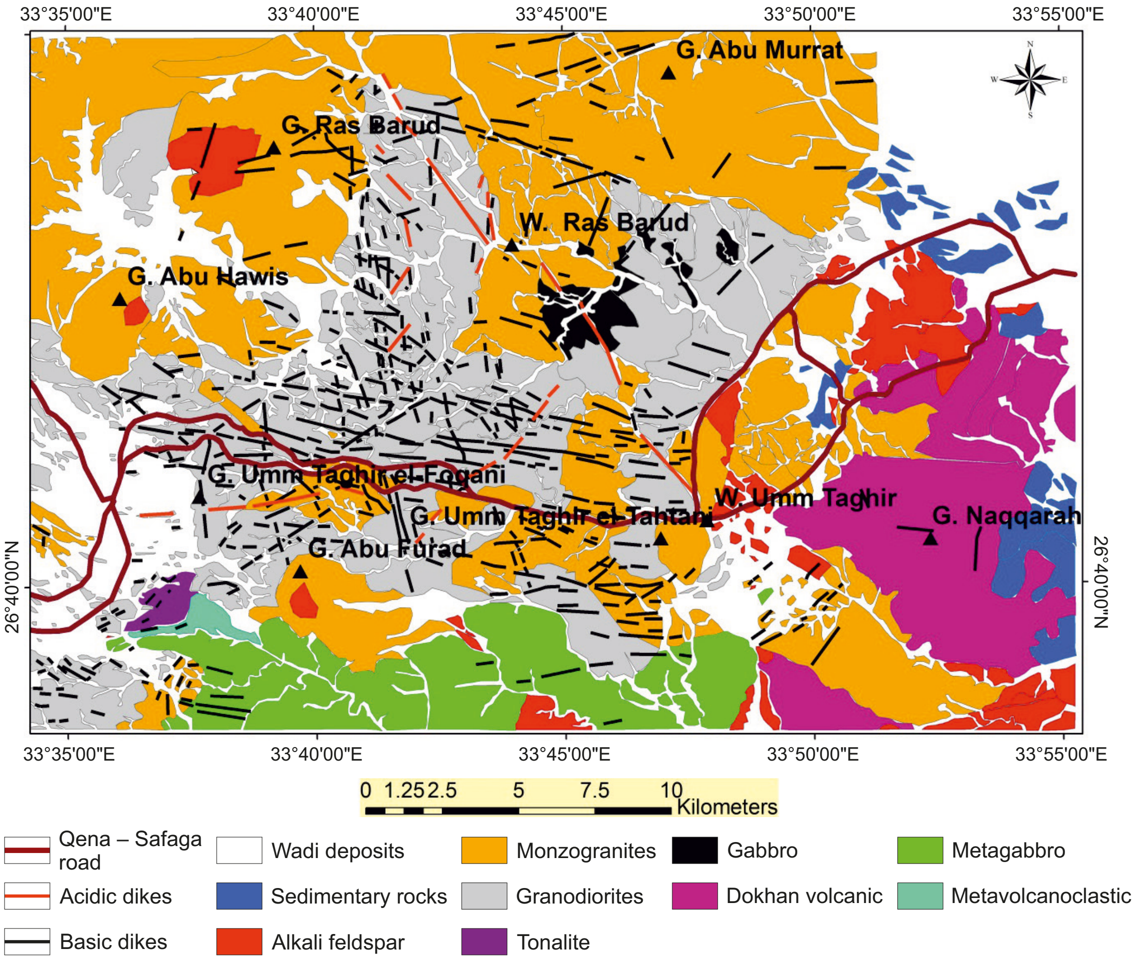

Fig. 5. Simplified geological map of the Um Taghir area, based on the data obtained by the integration of the remotely sensed data processing and field observations [Awad et al., 2022].

Рис. 5. Упрощенная геологическая карта района Ум Тагир, составленная на основе интеграции данных дистанционного зондирования и полевых наблюдений [Awad et al., 2022].

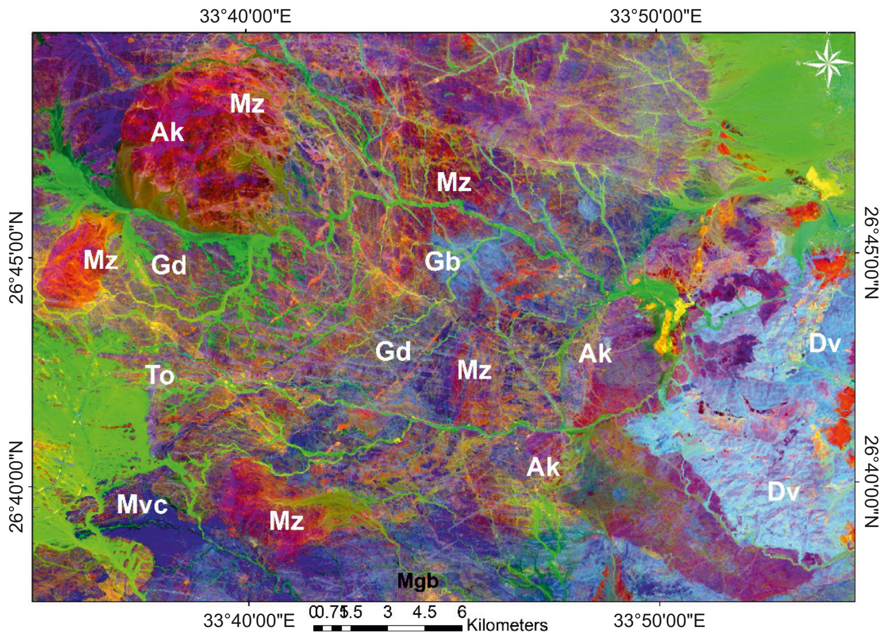

Fig. 6. Minimum noise fraction (3, 2, 1) of Sentinal-2A image of Um Taghir area.

Рис. 6. Минимальная доля шума (3, 2, 1) на изображении района Ум Тагир со спутника Sentinel-2A.

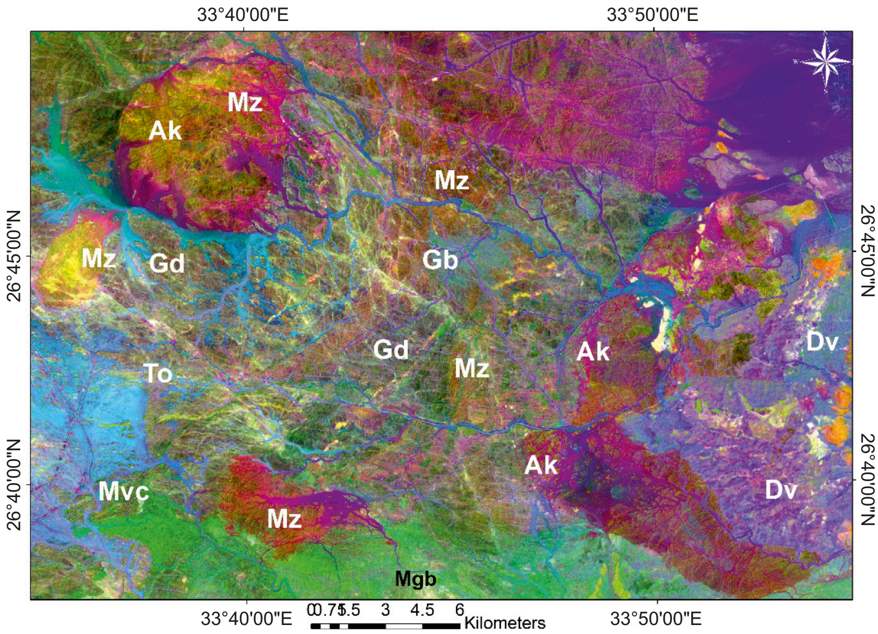

Fig. 7. Minimum noise fraction (3, 4, 2) of Sentinal-2A image of Um Taghir area.

Рис. 7. Минимальная доля шума (3, 4, 2) на изображении района Ум Тагир со спутника Sentinel-2A.

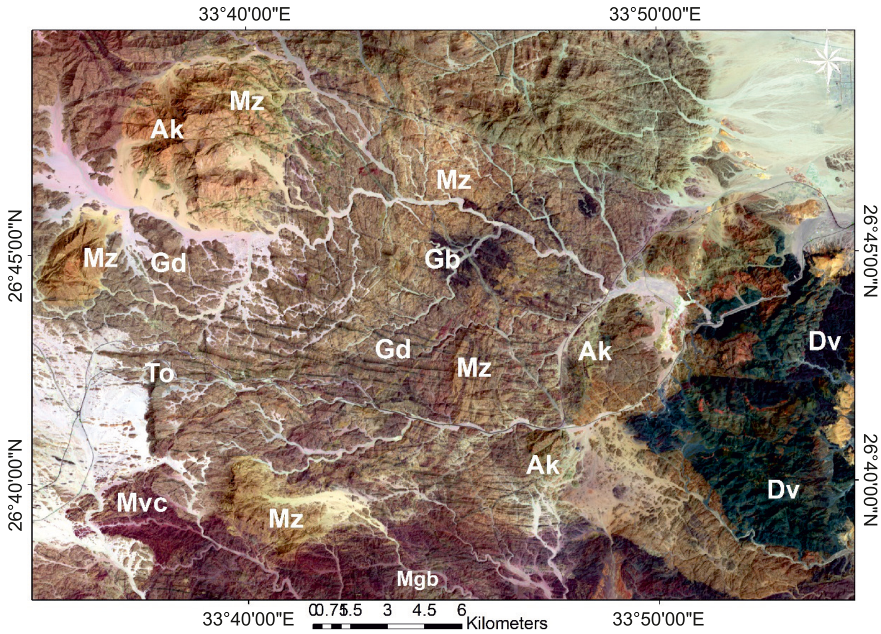

Fig. 8. FCC-derived image (12, 8, 2) of the Um Taghir area.

Рис. 8. Снимок района Ум Тагир в режиме FCC (12, 8, 2).

the false color composite image (12, 8, 2) which was used as a complement for geological mapping. These combinations attempted to select the best color composite image to extract meaningful information about visual lithological discrimination between the rock units studied (Fig. 8).

4.3. Principal Component Analysis (PCI)

The principal components analysis (PCA) is one of the most important image enhancement techniques, which separates noise components from the original data as well as reduces their dimensionality [Singh, Harrison, 1985]. Moreover, the PCA transformation identifies lithologic units more effectively than the other image enhancement techniques [Liu et al., 2014; Nair, Mathew, 2012; Amer et al., 2010].

According to the PCA's eigenvectors and eigenvalues statistics, the first principal component (PCA1) has high weighting compared to the other (PCA) bands. PCA1 accounts for 96.71 % of the data's total variance as seen above (see Table 1). The second PCA is PCA2, with a variance of about 2.27 % (Table 5). Based on eigenvector loadings for bands, the best PCA sections used in this study are PCA 2, PCA 1 and PCA 6 in (RGB). From the image interpretation, all granitic rocks in the study have relatively high reflectance in bands 1 and 2, and low reflectance in band 6, as well as metagabbro and metavolcanoclastic rocks have high reflectance in band 2 and low reflectance in bands 1 and 6. On the other hand, the gabbro and dokhan volcanic rocks are characterized by high reflectance in band 6 and low reflectance in bands 1 and 2. So, these PCA combinations are excellent at differentiating between different lithological units in the current study area.

The metagabbro and metavolcanoclastic rocks have violet color. The gabbro and dokhan volcanic rocks are characterized by blue color. Monzogranite shows reddish-gold, while Alkali granite exhibits bluish gold. The oldest granites are differentiated into two types, tonalite of brown color and granodiorite of gold color. Wadi deposits are shown in green, and the dikes have dark blue color (Fig. 9, a).

Another Sentinel-2A composite color of PCA bands (5, 1, 4) is found in RGB (Fig. 9, b). Based on this PCA composite image, the differentiation between lithological units have become clearer than that of the above PCA (2, 1, 6). Eigenvectors and eigenvalues of PCA (5, 1, 4) are high, so that all rock units in the study area can be easily detected and recognized. The metavolcanoclastic and metagabbro rocks are characterized by pink and reddish violet colors, while gabbro rocks have a violet color. Dokhan volcanic rock shows dark pink. The granitic rocks are differentiated into four types: tonalite (pink), gran-odiorite (light pink), monzogranite (green to greenish pink) and alkali granite (reddish gold); moreover, this PCA composite helped us to identify alkali granites in Gable Baroud.

5. ANALYSIS OF LINEAMENTS

The main goal of remote sensing is to make a profound contribution to structural mapping as it provides some information on spatial distribution and surface relief of structural

Table 5. Eigenvector matrix for ten Sentinel-2A bands

Таблица 5. Матрица собственных векторов для десяти полос захвата Sentinel-2A

Input Bands	Band 1	Band 2	Band 3	Band 4	Band 5	Band 6	Band 7	Band 8	Band 9	Band 10	Eigenvalues %
PCA 1	−0.315802	−0.316106	−0.316381	−0.316391	−0.316394	−0.316364	−0.316374	−0.316338	−0.315958	−0.31617	96.71
PCA 2	0.61172	0.44618	0.102988	0.059917	−0.044727	−0.111567	−0.061754	−0.177806	−0.519084	−0.30529	2.27
PCA 3	−0.357035	−0.13571	0.126292	0.198142	0.241493	0.334396	0.253667	0.291249	−0.366527	−0.58758	0.51
PCA 4	0.220373	−0.120372	−0.562733	0.223836	0.283103	0.277767	−0.57613	0.271417	−0.06823	0.051231	0.23
PCA 5	0.285087	−0.152581	−0.366344	−0.582909	0.040323	−0.002112	0.492972	0.361404	−0.184973	0.109423	0.14
PCA 6	0.192429	0.129673	−0.109906	−0.191806	−0.0334	−0.037976	−0.048833	0.094351	0.667812	−0.66142	0.055
PCA 7	0.227831	−0.409135	−0.146205	0.175801	0.502104	−0.059293	0.297534	−0.607927	−0.075507	0.09483	0.024
PCA 8	−0.047884	0.12719	−0.512984	0.577551	−0.446707	−0.152095	0.39818	0.036849	0.041829	−0.02186	0.019
PCA 9	0.277464	−0.51754	0.310655	0.256333	−0.055267	−0.548341	−0.085647	0.423075	−0.00744	−0.05326	0.014
PCA 10	−0.31708	0.420215	−0.171339	−0.013925	0.549525	−0.608045	0.002218	0.142759	−0.027172	0.022571	0.001

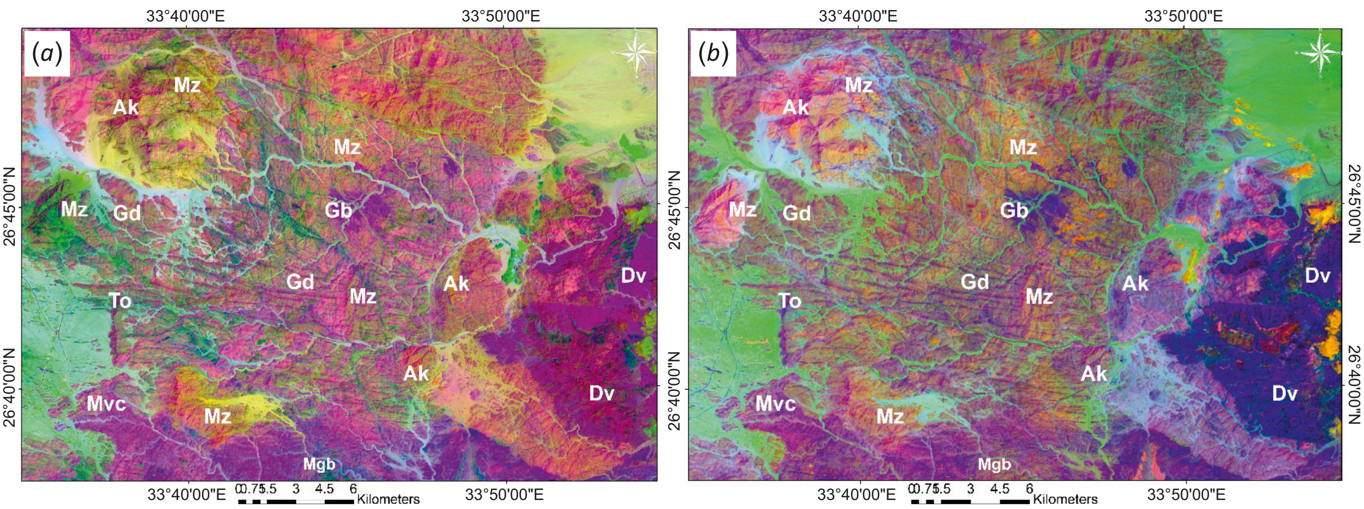

Fig. 9. Principal components analysis (*a*) – (2, 1, 6) in RGB; (*b*) – (5, 1, 4) in RGB of Sentinel-2A image of Um Taghir area.

Рис. 9. Анализ главных компонент изображения района Ум Тагир со спутника Sentinel-2A: (*a*) – (2, 1, 6) в RGB; (*b*) – (5, 1, 4) в RGB.

elements. The high-resolution Sentinal-2A data (10 m with scale 1:40000) and Aster DEM (30 m with scale 1:100000) were used to detect the various linear features in Um Taghir area. The automatic lineaments extraction from Sentinel-2A and ASTER DEM of the study area was carried out within the new PCI Geomatica package parameters proposed. The number and and length of lineaments of each ASTER DEM are calculated and tabulated from each band in each data type after correction, as given in (Table 6). The lineament features are interpreted as the result of the fieldwork and analysis of the Satellite images. The structure features include compressional and extensional forces resulting in thrusting, schistosity and folding, and lineament identification such as faults, joints, and dikes. The Sentinel-2A image used in the present paper consists of 13 bands with different spatial resolutions. High spatial resolution is 10 m, while low spatial resolution is 60 m. So, the lineaments were automatically extracted from high spatial resolution bands. In this study, a false color composite of bands 432 in the RGB with a high spatial resolution of 10 m was chosen to be used in lineament extraction, because band 4-3-2 with a spatial resolution of 10 m allows extracting much larger number of features (Fig. 10, a). Sobel edge detector was applied to FCC Sentinel-2A. The results of lineament extraction are based on of FCC FCC 432 Sentinel-2A image. The total lineament number and length of the Um Taghir area are 1067 and 577.02 km, respectively. Rose diagram shows that these lineaments' major trend has two directions, WNW – ESE and NE-SW, followed by those oriented NW-SE, N-S and E–W (Fig. 10, b). A lineaments density map was generated to highlight areas with the prevalence of structures. Thus, red represents areas with the highest prevalence, while green represents areas with the lowest prevalence

Table 6. Summarized numbers and lengths of lineaments extracted from each ASTER DEM in the Um Taghir area

Таблица 6. Суммарные количества и суммарные длины линеаментов, извлеченных из каждой ЦМР ASTER DEM района Ум Тагир

Sentinel-2A		Target	Number	Length (km)
		FCC 4-3-2	1067	577.02
Azimuth angles	1	0°	224	342.09
	2	45°	216	384.81
	3	90°	187	339.57
	4	135°	289	464.59
	5	180°	349	536.35
	6	225°	375	560.85
	7	270°	326	480.97
	8	315°	328	479.17
1		Faults	43	126.01
2		Dikes	506	301.58

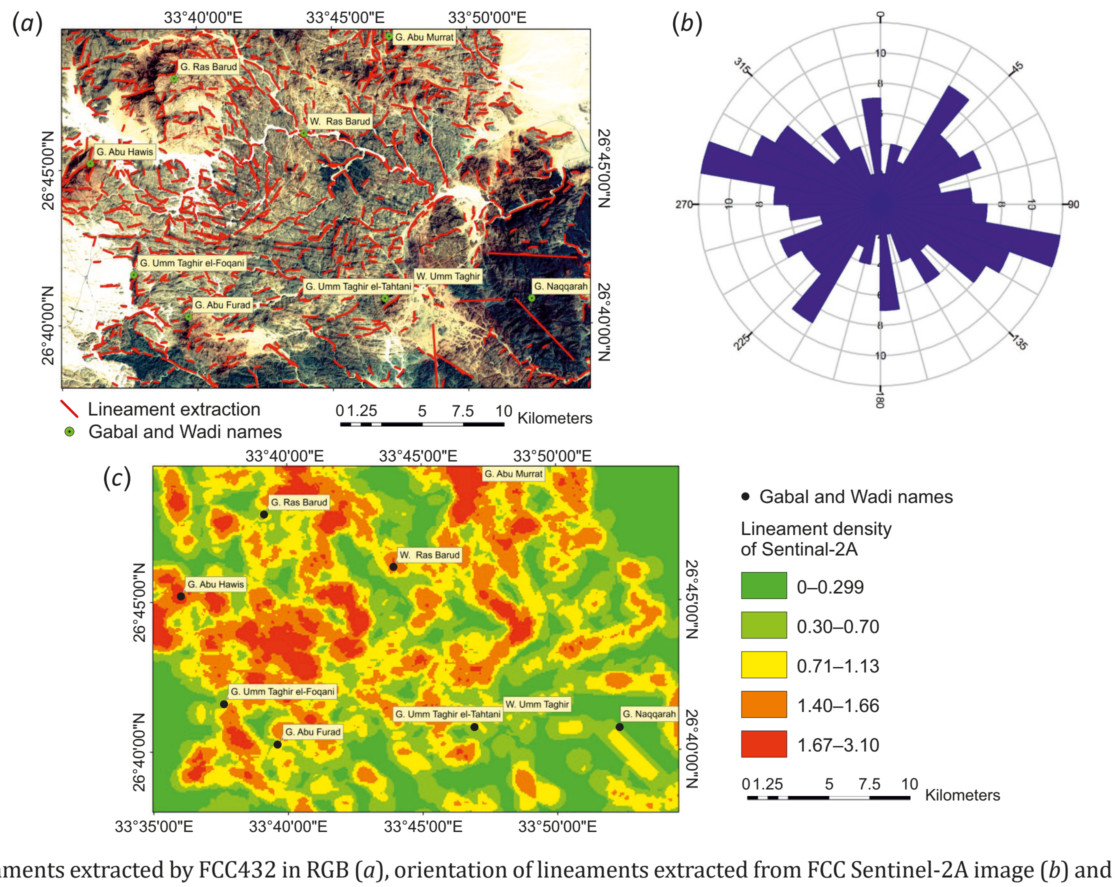

Fig. 10. Lineaments extracted by FCC432 in RGB (*a*), orientation of lineaments extracted from FCC Sentinel-2A image (*b*) and Lineament density classes and their areal extent (*c*).

Рис. 10. Линеаменты, извлеченные FCC432 в RGB (*a*), ориентация линеаментов, извлеченных из снимка Sentinel-2A в режиме FCC (*b*) и классы плотности линеаментов и их площадное распространение (*c*).

(Fig. 10, c). All lineament features in the study area were detected and extracted from Aster DEM. Consideration will be given to the Aster DEM eight separate shaded reliefs because of 30 m very high resolution. Each azimuth angle of the Aster DEM shaded relief has been studied separately, with numbers and length of the lineaments extracted and plotted on a rose diagram, to identify all trends in the study area. The intensity of the research activities is related to the need for extraction of Aster DEM's lineaments from as many azimuth angles as possible to obtain a more reliable image. The structural lineament density map has been created to show the concentration and prevalence of the structures in the study atrea in the context of numbers and lengths for each Aster DEM layer and Sentinel-2A image. At 0° shaded relief (Fig. 11, a), computations were made of about 224 lineament features 342 km in length, with statistical analysis performed on their orientations (Fig. 11, b). The lineament length density map for the study area shows a variation range; from 0 to 5.67 km per sq. km (Fig. 11, c). According to rose diagrams (Fig. 11, d), the two trends that control the entire region's topographic lineaments are those striking NNW – SSE and N-S.

On the shaded-relief image (azimuth angle of 45°) (Fig. 12, a) the number of lineament features is 216. Their length was calculated to be 384.8 km, and their directions were statistically interpreted (Fig. 12, b). On the other hand, the lineament length density computed for the study area at 45° azimuth angle varies from 0 to 8.52 per sq. km. (Fig. 12, c). The theoretical interpretation of rose diagrams (Fig. 12, d) allowed us to conclude that the two trends controlling the topographic lineaments in the studied area are those striking NWSE and NNW – SSE.

There were one hundred eighty-seven lineament features that were extracted and computed at 90° azimuth angle (Fig. 13, a); the total length of these lineaments is 339.6 km, and their main directions were calculated based on statistical deduction (Fig. 13, b). There has been a lineament length density map made of the study area. It indicates that the density values vary in the range 0 to 9 per sq. km (Fig. 13, c). According to rose diagrams (Fig. 13, d), the topographic lineaments are controlled by three trends striking NNE – SSW, NNE – SSW, and N-S.

On the shaded-relief image (azimuth angle of 135°) (Fig. 14, a), the number of lineament features was calculated to be 289, with a total length of 464.6 km; on the other hand, the orientations of lineament features were statistically analyzed (Fig. 14, b). This layer's lineament length density in the studied region has been mapped, varying from 0 to 10.58 km per sq. km (Fig. 14, c). The rose diagram plotting this layer shows that the topographic lineaments in this

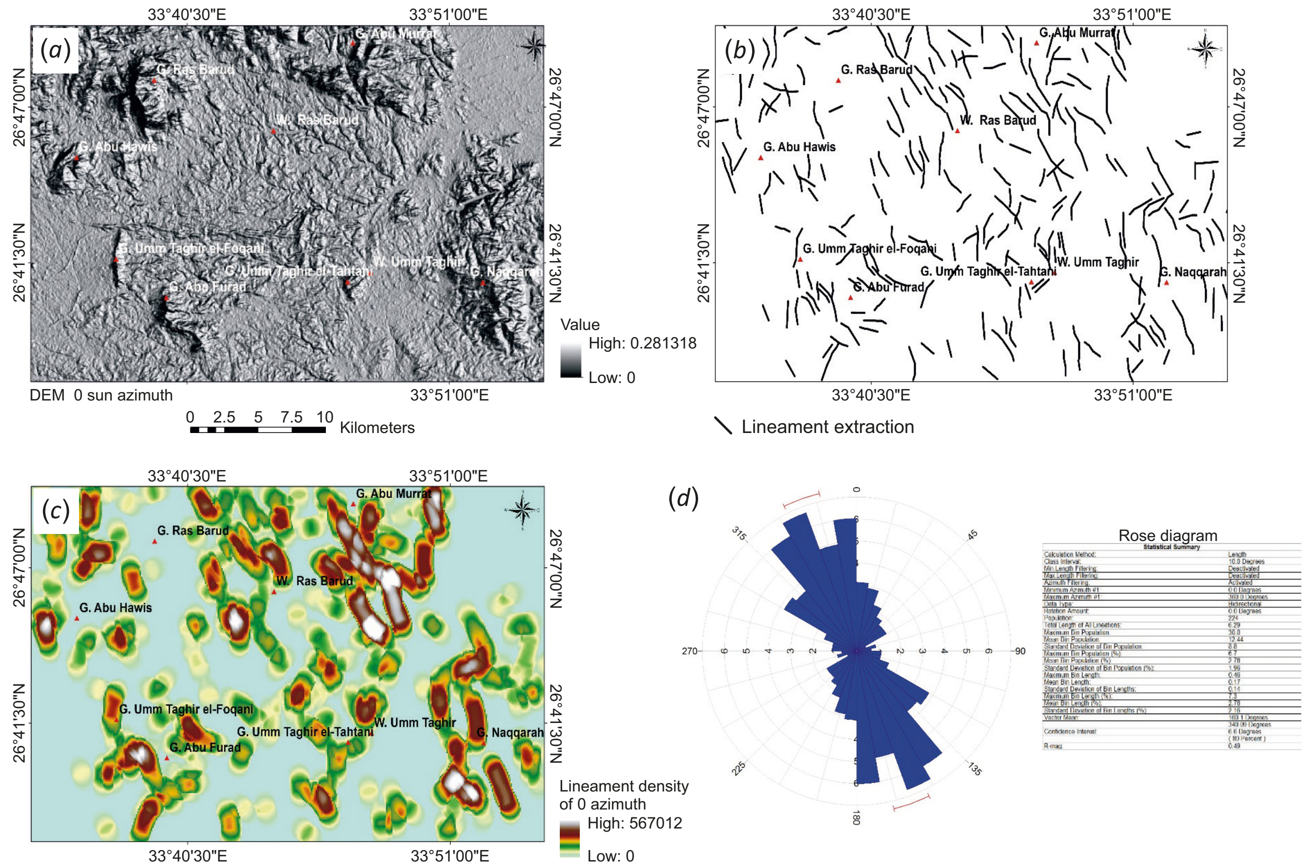

Fig. 11. 0° Azimuth angle (*a*), lineaments extracted by 0° Azimuth angle (*b*), lineament density classes and their areal extent (*c*) and orientations of lineaments extracted from ASTER DEM (*d*).

Рис. 11. Азимутальный угол 0° (*a*), линеаменты, извлеченные при азимуте 0° (*b*), классы плотности линеаментов и их площадное распространение (*c*) и ориентация линеаментов, извлеченных с помощью использования ASTER DEM (*d*).

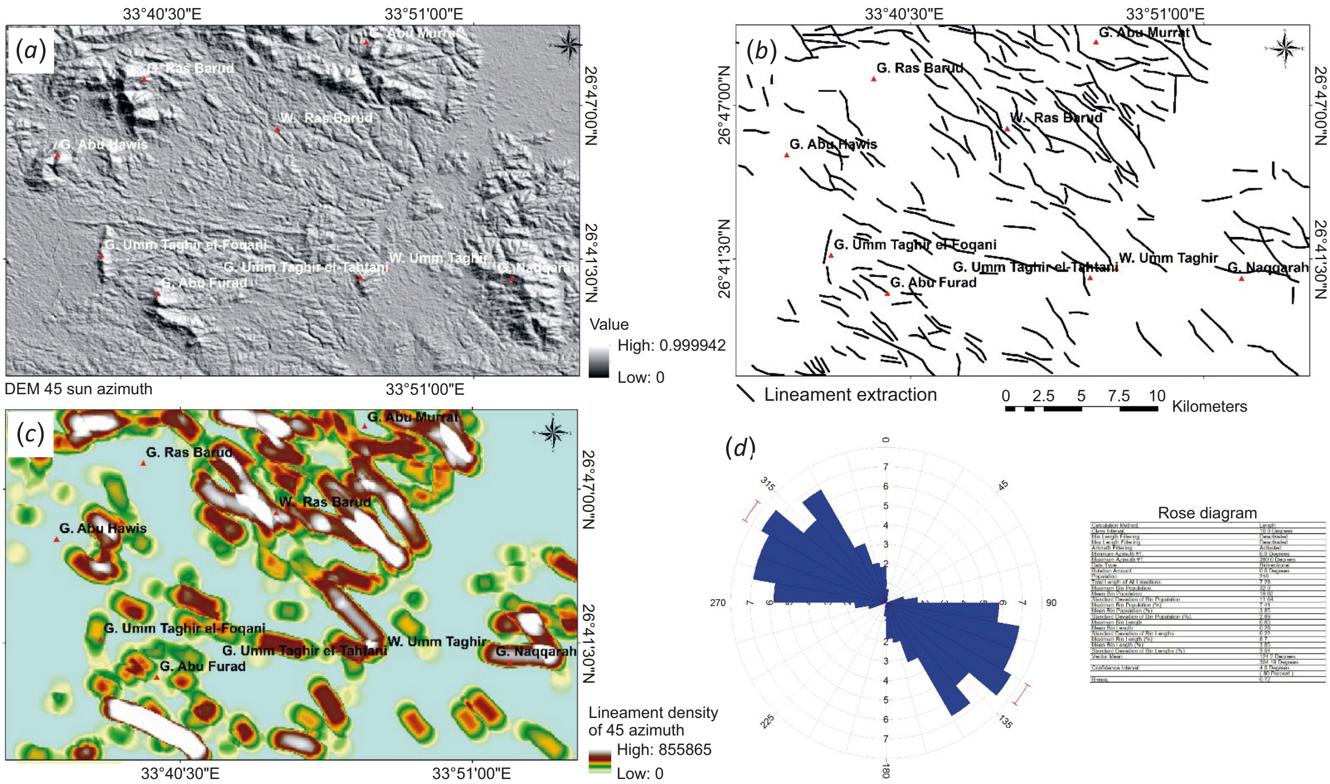

Fig. 12. 45° Azimuth angle (*a*), lineaments extracted by 45° Azimuth angle (*b*), lineament density classes and their areal extent (*c*) and orientation of lineaments extracted from ASTER DEM (*d*).

Рис. 12. Азимутальный угол 45° (*a*), линеаменты, извлеченные при азимуте 45° (*b*), классы плотности линеаментов и их площадное распространение (*c*) и ориентация линеаментов, извлеченных с помощью использования ASTER DEM (*d*).

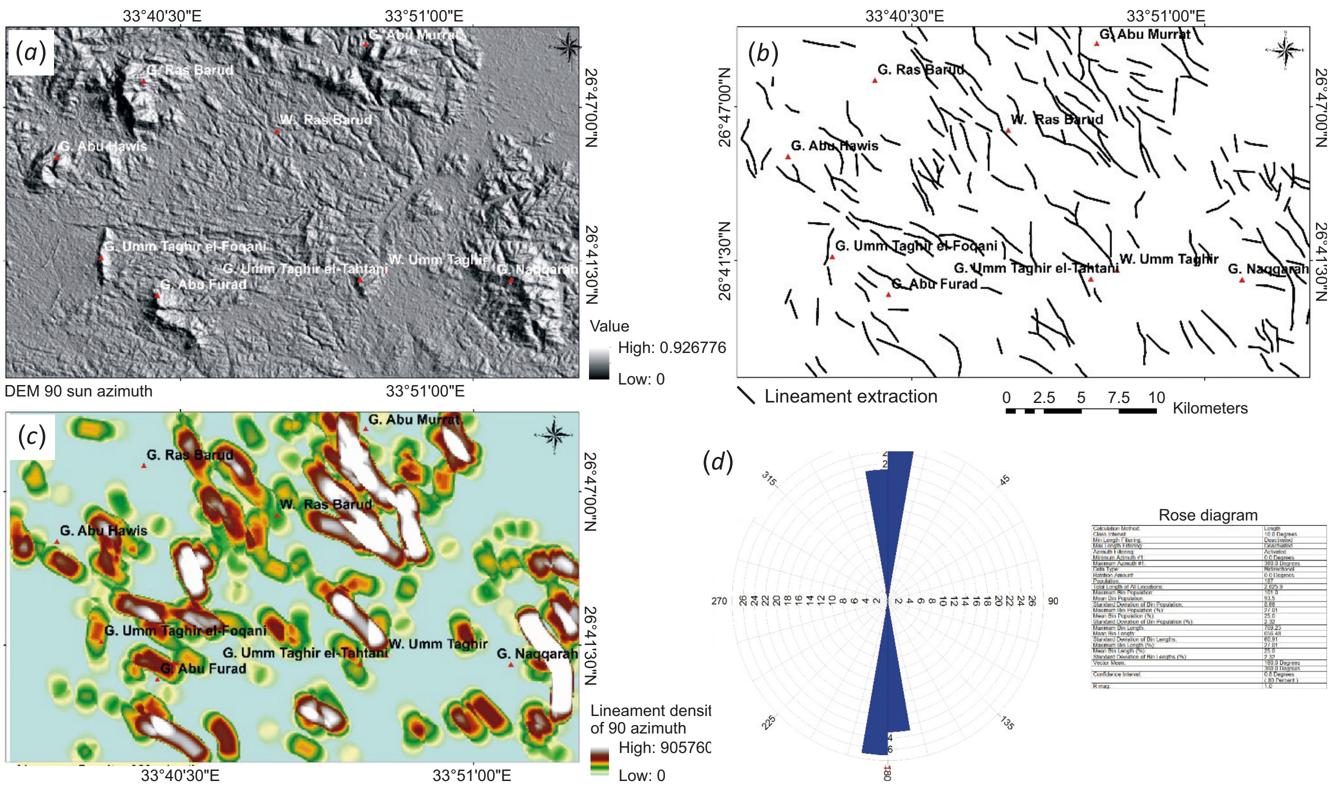

Fig. 13. 90° Azimuth angle (*a*), lineaments extracted by 90° Azimuth angle (*b*), lineament density classes and their areal extent (*c*) and orientations of lineaments extracted from ASTER DEM (*d*).

Рис. 13. Азимутальный угол 90° (*a*), линеаменты, извлеченные при азимуте 90° (*b*), классы плотности линеаментов и их площадное распространение (*c*) и ориентация линеаментов, извлеченных с помощью использования ASTER DEM (*d*).

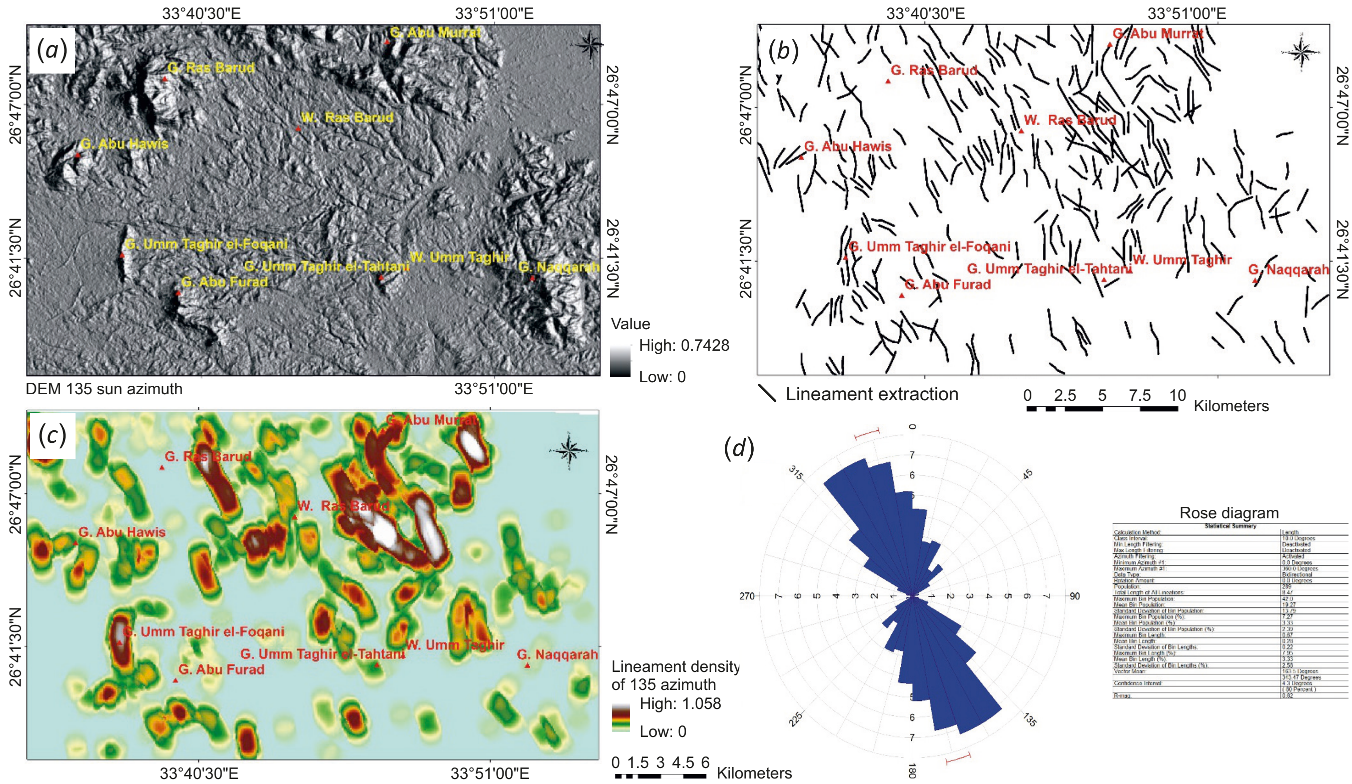

Fig. 14. 135° Azimuth angle (*a*), lineaments extracted by 135° Azimuth angle (*b*), lineament density classes and their areal extent (*c*) and orientations of lineaments extracted from ASTER DEM (*d*).

Рис. 14. Азимутальный угол 135° (*a*), линеаменты, извлеченные при азимуте 135° (*b*), классы плотности линеаментов и их площадное распространение (*c*) и ориентация линеаментов, извлеченных с помощью использования ASTER DEM (*d*).

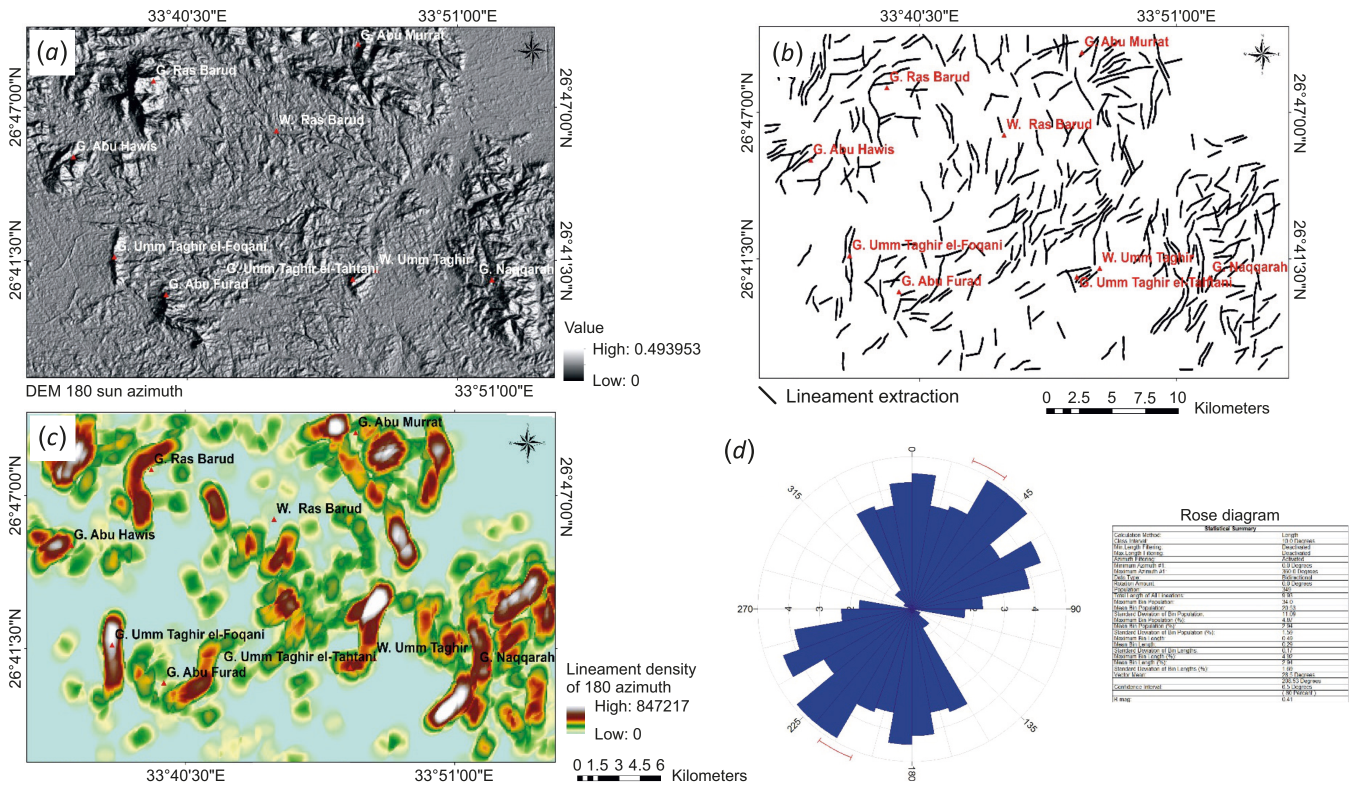

Fig. 15. 180° Azimuth angle (*a*), lineaments extracted by 180° Azimuth angle (*b*), lineament density classes and their areal extent (*c*) and orientations of lineaments extracted from ASTER DEM (*d*).

Рис. 15. Азимутальный угол 180° (*a*), линеаменты, извлеченные при азимуте 180° (*b*), классы плотности линеаментов и их площадное распространение (*c*) и ориентация линеаментов, извлеченных с помощью использования ASTER DEM (*d*).

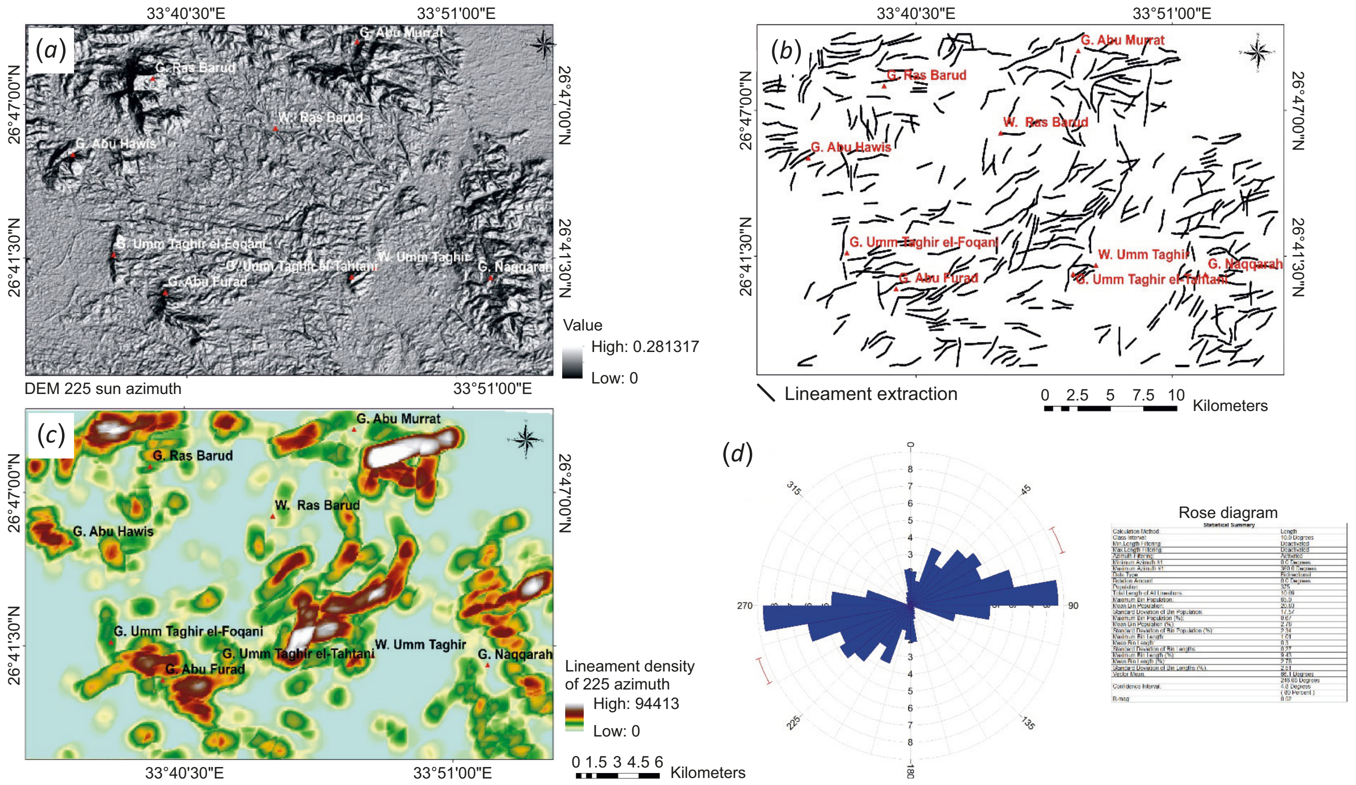

Fig. 16. 225° Azimuth angle (*a*), lineaments extracted by 225° Azimuth angle (*b*), lineament density classes and their areal extent (*c*) and orientations of lineaments extracted from ASTER DEM (*d*).

Рис. 16. Азимутальный угол 225° (*a*), линеаменты, извлеченные при азимуте 225° (*b*), классы плотности линеаментов и их площадное распространение (*c*) и ориентация линеаментов, извлеченных с помощью использования ASTER DEM (*d*).

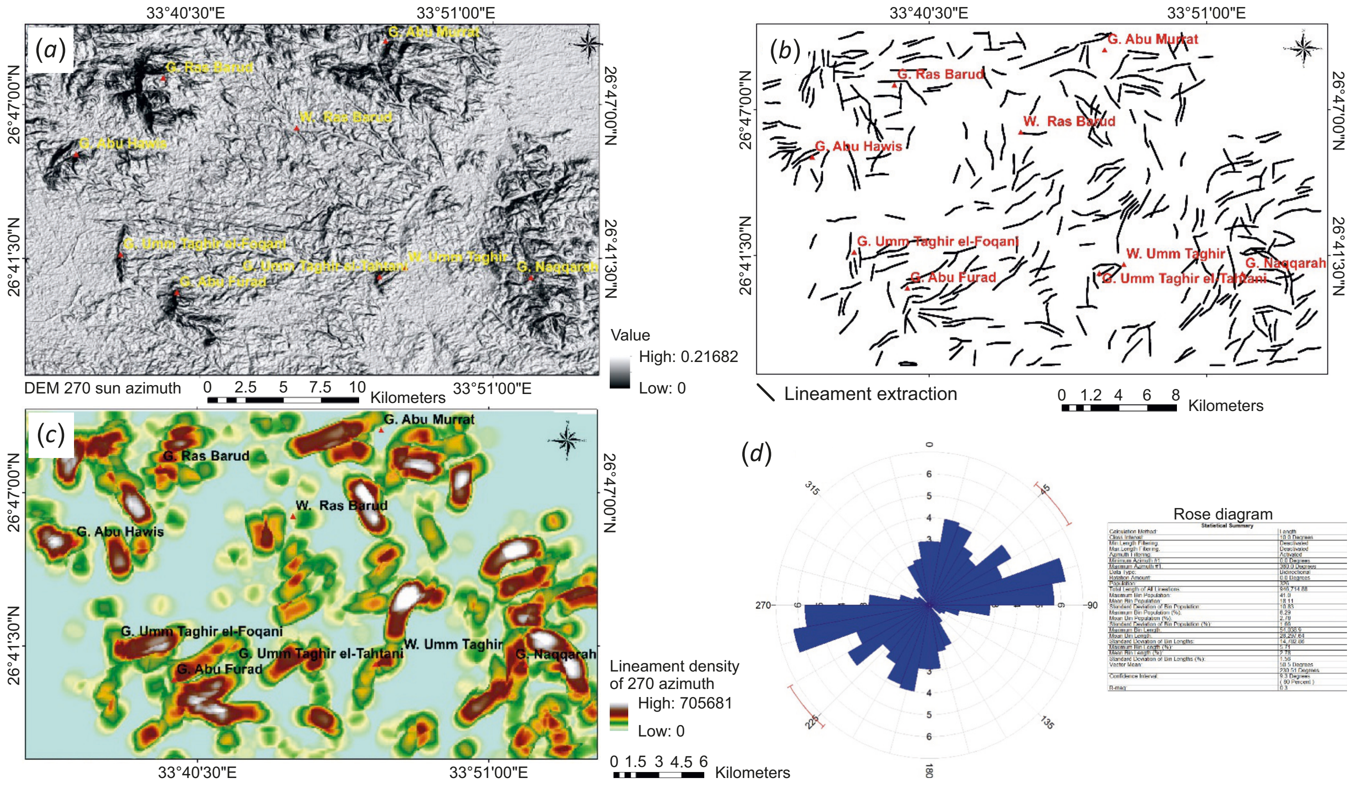

Fig. 17. 270° Azimuth angle (*a*), lineaments extracted by 270° Azimuth angle (*b*), lineament density classes and their areal extent (*c*) and orientations of lineaments extracted from ASTER DEM (*d*).

Рис. 17. Азимутальный угол 270° (*a*), линеаменты, извлеченные при азимуте 270° (*b*), классы плотности линеаментов и их площадное распространение (*c*) и ориентация линеаментов, извлеченных с помощью использования ASTER DEM (*d*).

area are controlled by two trends striking NNW – SSE and NW-SE (Fig. 14, d).

On the shaded-relief image (azimuth angle of 180°) (Fig. 15, a), we could calculate about 349 lineament features, with a total length of 536.4 km and statistically interpreted orientations (Fig. 15, b). The calculated densities of the lineament length for this layer in the study area range from 0 to 8.47 km per sq. km (Fig. 15, c). In accordance with the interpretation of rose diagrams (Fig. 15, d), the topographic lineaments are entirely controlled by two regional trends striking NW-NE – SW-SE and NE-SW.

On the shaded-relief image (azimuth angle of 225°) (Fig. 16, a), there were computed 375 lineament features, with a total length of 560.85 km and orientations statistically extracted (Fig. 16, b). This layer's lineament length density in the study area has been mapped, varying from 0 to 9.44 km per sq. km (Fig. 16, c). Rose diagrams (Fig. 16, d) showed that the two trends controlling the topographic lineaments in the entire region are striking NNE-SSW and NE-SW.

On the shaded-relief image (azimuth angle of 270°) (Fig. 17, a), there were calculated about 326 lineament features, with a total length of 481 km and specific orientations statistically analyzed (Fig. 17, b). The lineament length density in the region has been mapped, varying from 0 to 7 km per sq. km (Fig. 17, c). Based on the rose diagrams (Fig. 17, d), the two trends that control the topographic lineaments in the entire region are those striking NE-NW – SE-SW and NE-SW.

The final shaded-relief image at azimuth angle of 315° (Fig. 18, a) includes 328 lineament features, with a total length of 479.167 km and orientations statistically analyzed (Fig. 18, b). The lineament length density of this layer in the study area has been mapped, varying from 0 to 7 km per sq. km (Fig. 18, c). Rose diagrams (Fig. 18, d) show that two trends controlling the topographic lineaments in the entire region are those striking NNW – SSE and NW-SE.

5.1. Compressional features

Compressional structure features include many geologic structures such as thrusting, schistosity and folding that result from the arc compression force– the arc accretion phase had been affected throughout the Arabian – Nubian Shield at 750–650 Ma, while the strike-slip movement is related to the latter stage of the arc accretion event [Vail, 1983; Abdelsalam, Stern, 1996].

Thrust faults. Thrusts are entirely affected by the NE–SW compressional force at the southern margins; on the other hand, the older metavolcanoclastic rock units are thrust over the younger metagabbro rock units, as well as the metagabbro rocks in the extreme south of the study area are thrust over the granodiorite rocks (Fig. 19, a). Highly

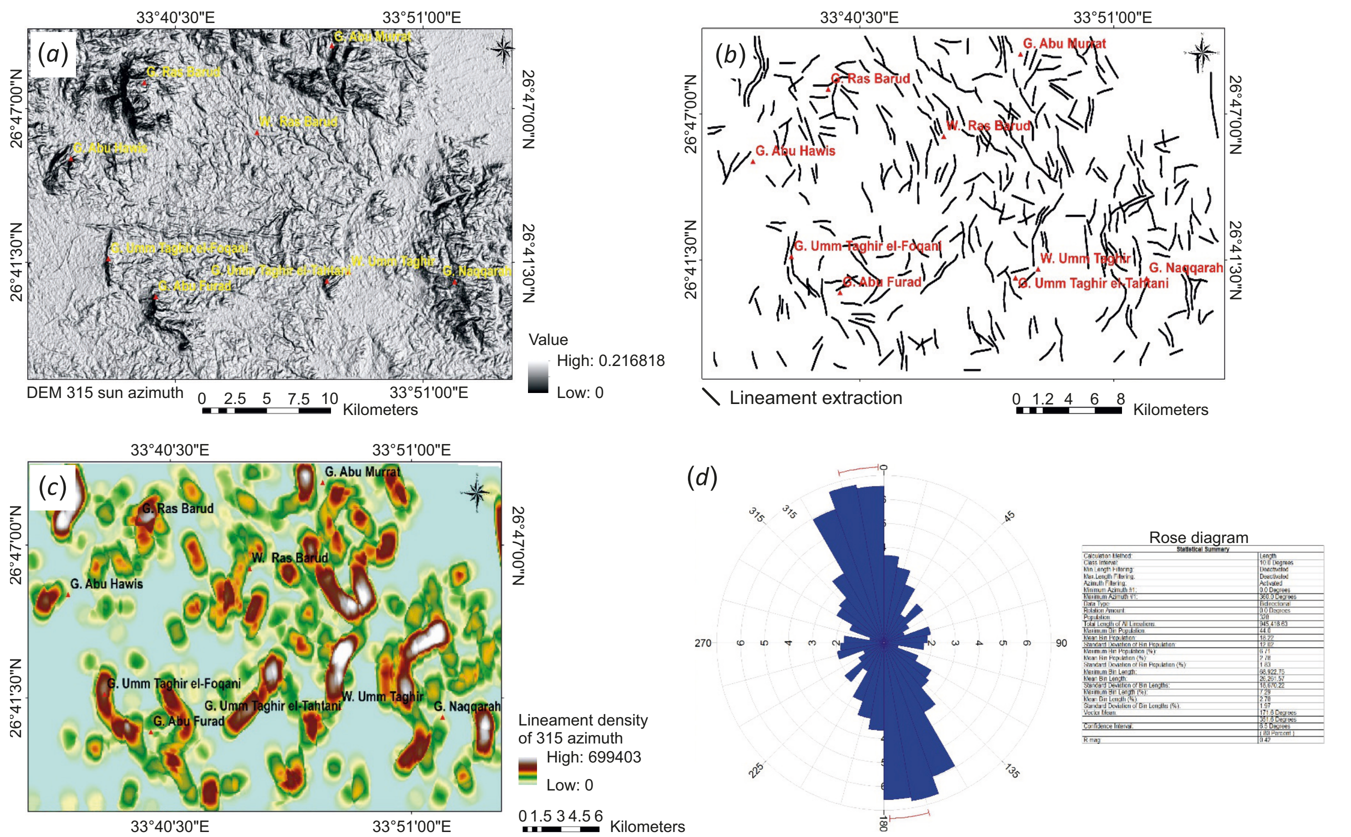

Fig. 18. 315° Azimuth angle (*a*), lineaments extracted by 315° Azimuth angle (*b*), lineament density classes and their areal extent (*c*) and orientations of lineaments extracted from ASTER DEM (*d*).

Рис. 18. Азимутальный угол 315° (*a*), линеаменты, извлеченные при азимуте 315° (*b*), классы плотности линеаментов и их площадное распространение (*c*) и ориентация линеаментов, извлеченных с помощью использования ASTER DEM (*d*).

deformed and cataclastic rocks are found along the thrust zone. Another thrust fault in the study area is located on the northern side of Qena-Safaga road. The metavolcanoclastic rocks show pronounced schistosity with NE and NW trends and a dip varying from about 25° NE to 50° SW. There occur layering and sheeting, particularly in the metavolcanoclastic rocks (Fig. 19, b).

Folding. The Um Taghir synclinal fold is a major folded structure at the southern part of the study area. It was formed mostly due to elastic properties of metavolcanoclastic rock; E-W axial plane indicates that N-S compressional stress was subjected to the study area (Fig. 20, a, b).

5.2. Tensional features

Normal faults. Normal faults are abundant and common in the study area. They dissect almost all the mapped rock units (Fig. 21, a); rose diagram of normal faults indicates that the predominant trends of faults in the area are NE-SW and WNW – ESE, while E-W trend is less common (Fig. 21, b, c). A number of features such as displacement of dikes and drainage alignment observed therein occurred due to various forces affecting different rock units.

Joints. Joints are recorded due to tension force acting on a rock mass. Generally, they are well-defined in all the rocks investigated, mostly. Joints have NE, NNW, NW, SW and N-S trends. Granites show three sets of joints (Fig. 22, a). Exfoliation in granite and gabbro is common in the study area (Fig. 22, c, d). On the other hand, columnar joints are observed mainly in the Dokhanvolcanic porphyry at the Qena-Safaga Road. Metavolcanoclastic rock is confined to the southern part of the study area and affected by high-joint sets mainly trending NE-SW (Fig. 22, b).

5.3. Shear structure features

Strike-slip movement. Differently scaled strike-slip faults are common in the Wadi Um Taghir area. They can easily be recognized on the Sentinel-2A satellite image and observed in the field (Figs. 23, 24).

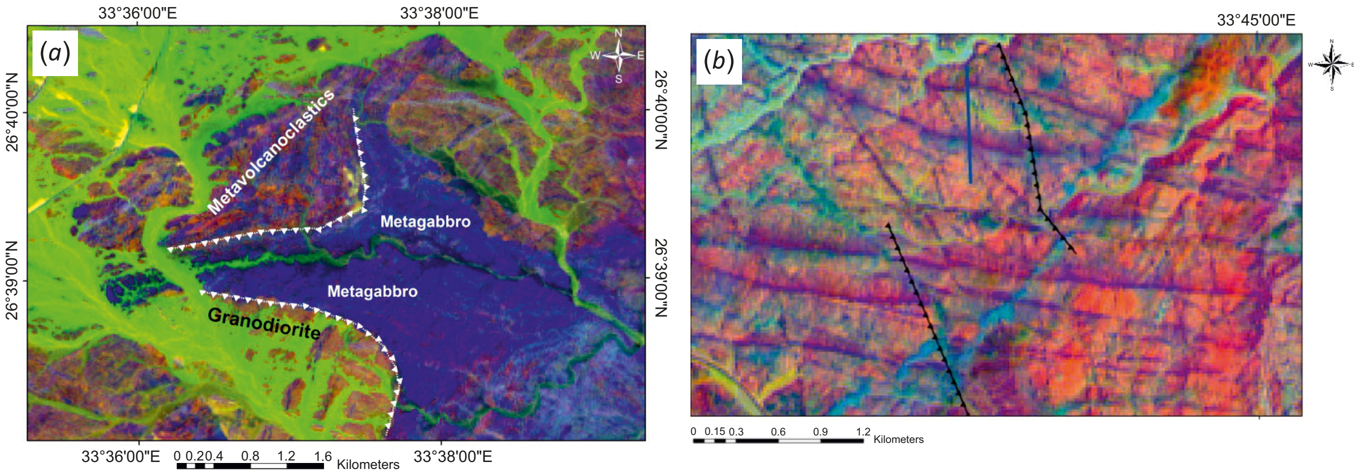

Fig. 19. Sentinel-2A image showing thrust faults in the study area.

Рис. 19. Снимок надвиговых разломов на изучаемой территории со спутника Sentinel-2A.

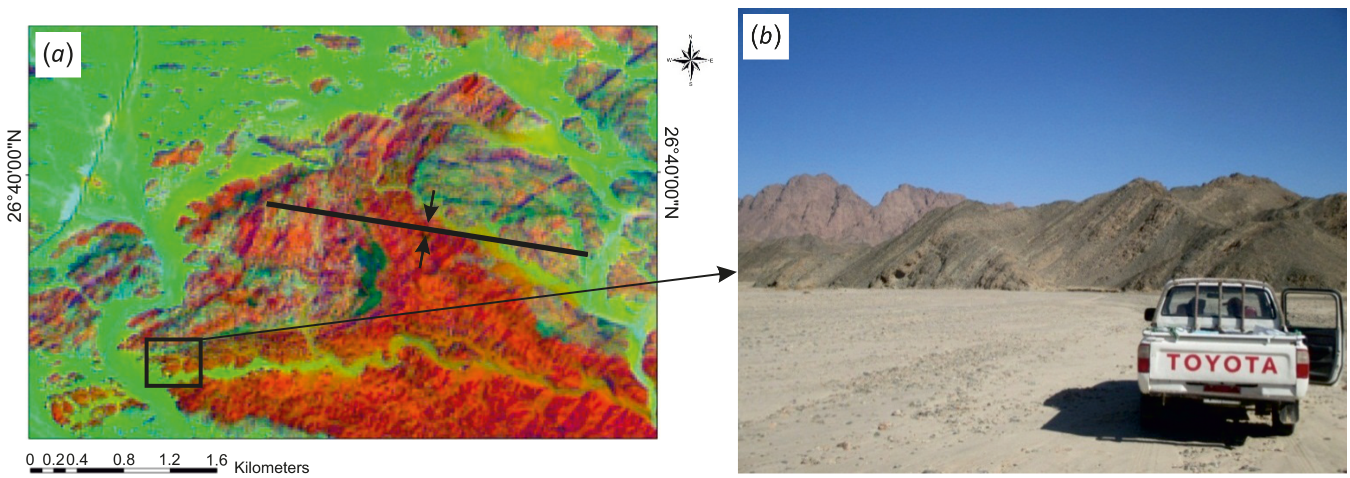

Fig. 20. Sentinel-2A image (*a*) and Field photograph showing synclinal fold in Um Taghir area (*b*).

Рис. 20. Снимок синклинальной складки в районе Ум Тагир со спутника Sentinel-2A (*a*) и фотография синклинальной складки в районе Ум Тагир, сделанная в полевых условиях (*b*).

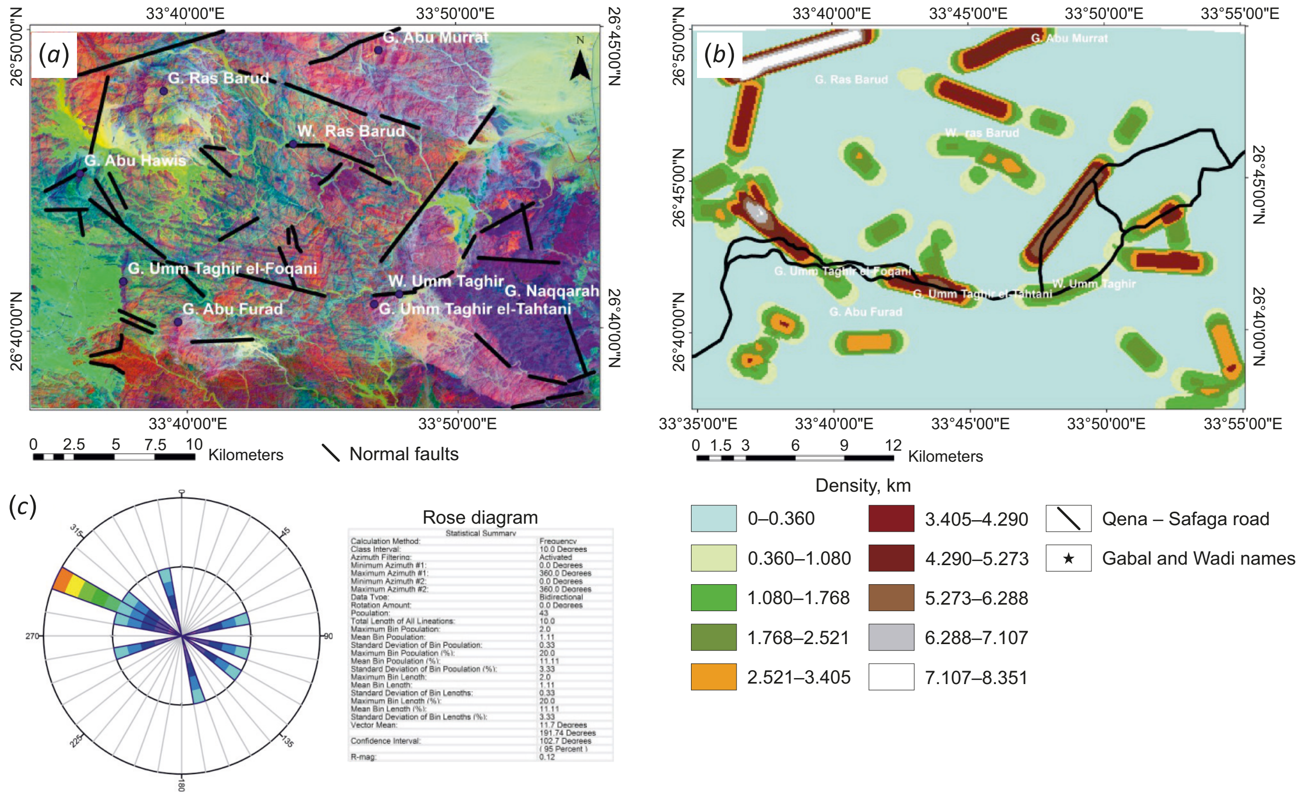

Fig. 21. Structural fault types in the study area (*a*), faults density classes and their areal extent (*b*) and rose diagram of fault types (*c*).

Рис. 21. Типы структурных разломов на изучаемой территории (*a*), классы плотности разломов и их площадное распространение (*b*) и роза-диаграмма типов разломов (*c*).

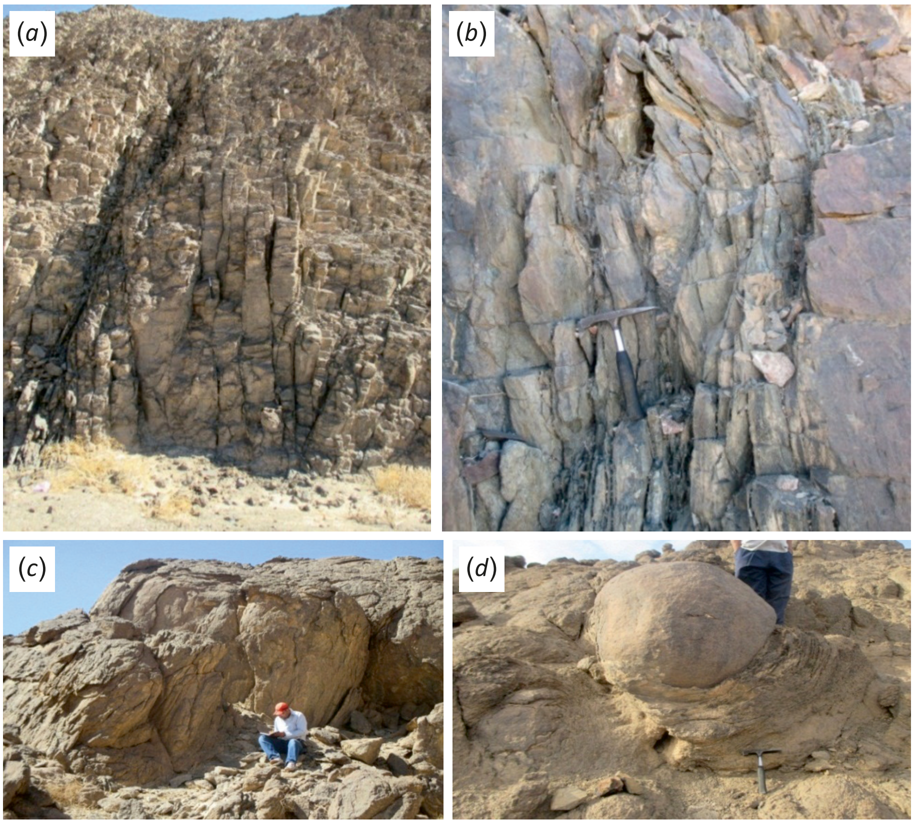

Fig. 22. Field photographs showing joint types in Um Taghir area.

Рис. 22. Фотографии типов трещин в районе Ум Тагир, сделанные в полевых условиях.

The Wadi Al Baroud area is an area of left-lateral strike-slip faults which trend WNW – ESE with about 1.6 km horizontal displacement. The northern part of the Gable Al Baroud granodiorites is displaced laterally about 1 km east (see Fig. 23, a). This movement has produced an opportunity to observe many features, such as some tilted dikes and fractured monzogranites. At the southwestern part of the study area in Gable Abu Furad metavolcanoclastic and metagabbro rocks undergo left-lateral strike-slip faulting with a lateral displacement of about 600 m and a width of about 250 m (see Fig. 23, b). The left-lateral strike-slip faults in the studied area trend NW-SE and E-W.

On the other hand, the right-lateral strike-slip faults are common and clearly defined at the Qena-Safaga road. The lateral displacement along the fault is about 2.5 km (Fig. 24, a). Another dextral strike-slip fault in the study area is located at the eastern part of the study area in Gable Nakkara. The length of the fault is about eight km based on the Sentinal-2A image and Google Earth Pro. The lateral displacement is 1.5 km towards EW (Fig. 24, b). However, the right lateral strike-slip faults mainly trend E-W, N-S and NNE-SSW.

5.4. Dikes and veins

Dikes and veins of different shapes and compositions, invading the older rocks, are easily interpreted on the Landsat image by their colour, tone, contrast, linear shape, and field relationships. Dikes are widely distributed in the mapped area, particularly in the granitic rocks, and stretch in different directions (Fig. 25, a). The density map of these dikes shows that they are concentered in the middle part of the study area (Fig. 25, b). They have different compositions and thicknesses, and are more resistant than country rocks. Based on the study area's dikes' rose diagram, the predominant trends are WNW – ESE and NW-SE, with minor trends directed E-W and N-S (Fig. 25, c). Dikes range in thickness from 30 cm to about 15 m and extend about 10 km. They comprise basic, intermediate, and acidic sets represented by basalts, andesites, and granites (Fig. 25, d). It has been noted that some of these dikes are tilted, which is

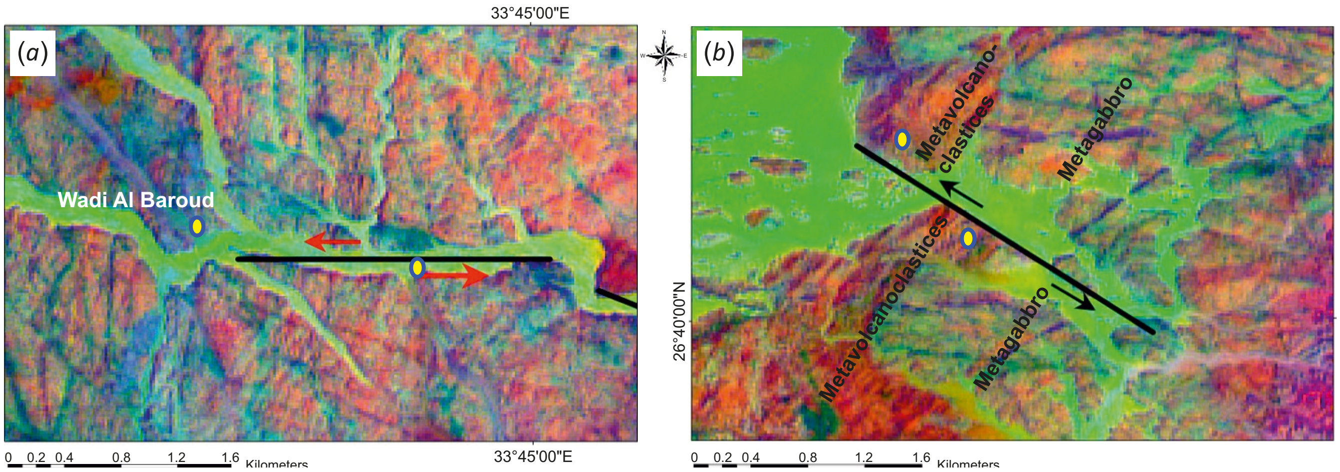

Fig. 23. Sentinel-2A image showing left-lateral strike-slip faults in the study area.

Рис. 23. Снимок левосторонних сдвиго-сбросов на изучаемой территории со спутника Sentinel-2A.

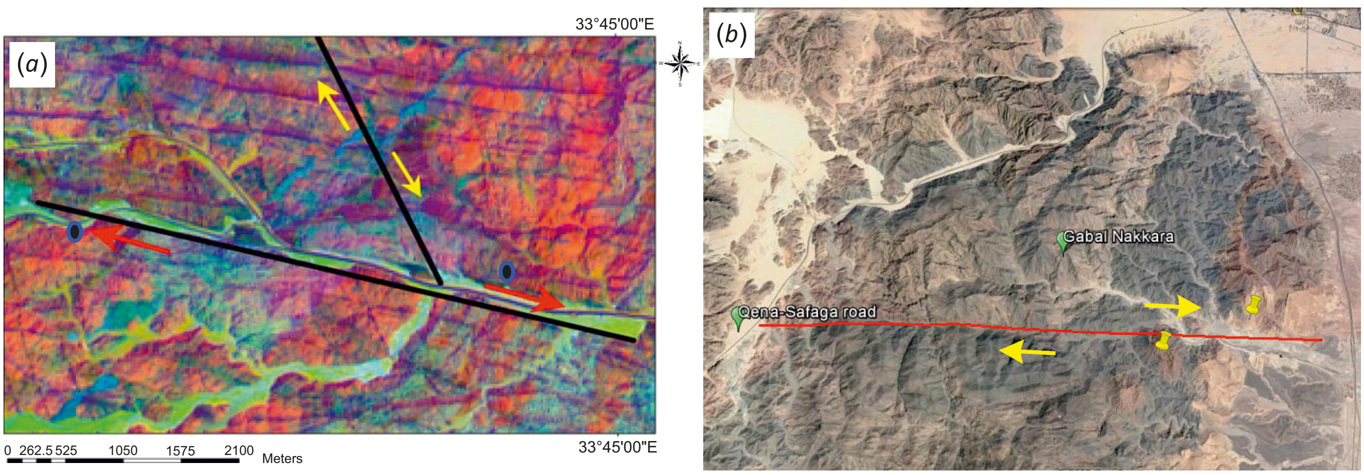

Fig. 24. Sentinel-2A image showing right-lateral strike-slip faults in the study area.

Рис. 24. Снимок правосторонних сдвиго-сбросов на изучаемой территории со спутника Sentinel-2A.

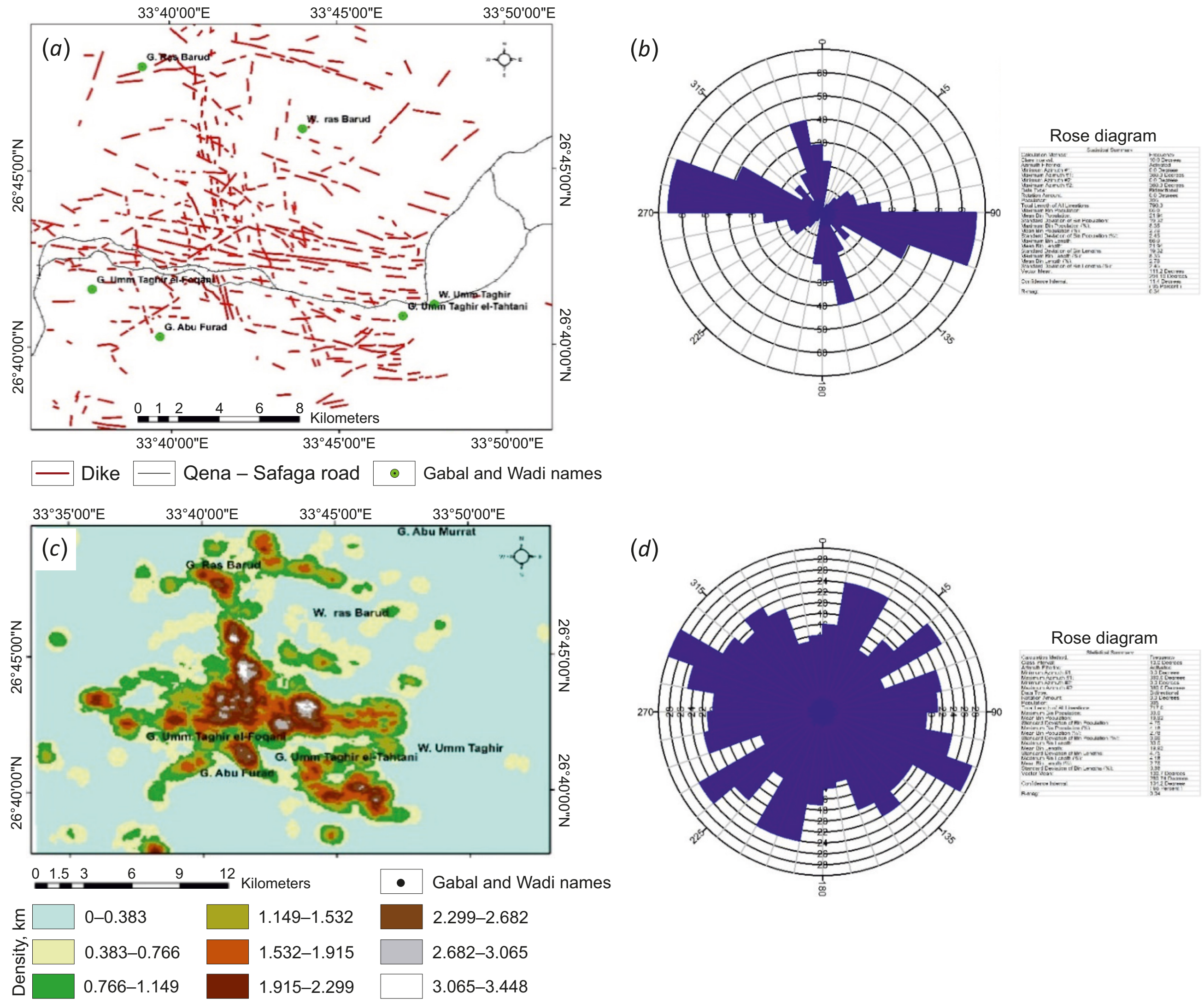

Fig. 25. Dike types in the study area (*a*), rose diagram of dike types (*b*), dike density classes and their areal extent (*c*) and rose diagram showing the length of all dike types (*d*).

Рис. 25. Типы даек на изучаемой территории (*a*), роза-диаграмма типов даек (*b*), плотность даек и их площадное распространение (*c*) и роза-диаграмма длины даек всех типов (*d*).

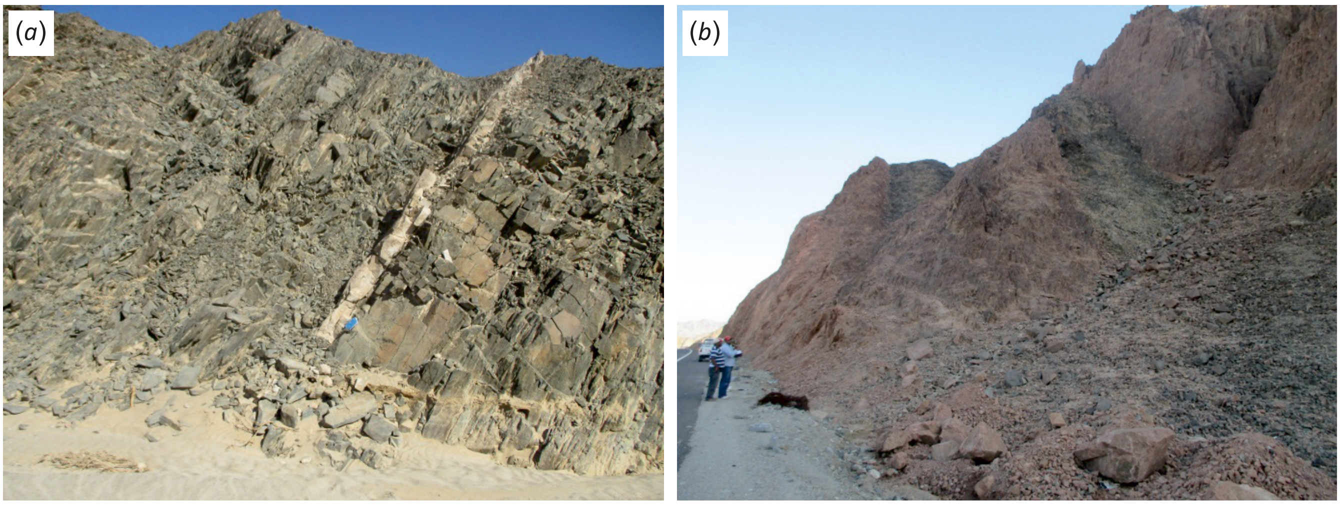

Fig. 26. Field photographs showing some acidic and basic dikes cutting in the rocks in the study area.

Рис. 26. Фотографии кислых и базитовых даек, секущих породы на изучаемой территории, сделанные в полевых условиях.

probably due to the EW strike-slip movement affected the alkali feldspar granite of Abu Hawies, Al Baroud and Um Taghir (Fig. 26).

6. CONCLUSION

The Um Taghir area is confined to the extreme northern boundary of the central Eastern Desert of Egypt at the west of Safaga City. This is one of the Neoproterozoic components of the North Arabian–Nubian Shield that was constrained to the East African Orogen (EAO) during the consolidation of Gondwana-through the accretion of plateaus. The Um Taghir area is covered by the island-arc and the late-to-post-magmatic rocks. The lineament density is high in the areas closer to the Wadi Um Taghir (Qena-Safaga road), with the maximum lineament density parallel to the trend of the Qena-Safaga shear zone. The analysis of the study area lineaments (as can be inferred from later accounts shows that they are stretching in different directions reflecting the multiple episodes of deformation events that occurred in the area over geological time. However, despite the variety of trends, there occurs the dominance of the NW-SE, WNW – ESE, N-S and NE-SW directions, followed by the trends directed EW and NNW – SSE. An abundance of tectonic and geological events in the study area gave rise to the formation of many lineament features as dikes and faults. From this standpoint, there have been monitored and identified some fractures that fill magmatic swarms like dikes and veins, mostly in the WNW direction and near the Qena-Safaga shear zone. It is worthy of note that these lineaments have a profound impact on the granite rocks, especially granodiorites. Therefore, it was concluded that migmatized granodiorites of the Wadi Al-Baroud area and those extending to the north, at Gable Abu Murrat, are oriented NW-WNW and show intensive growth near the contact zone affected by granodiorite dikes.

7. CONTRIBUTION OF THE AUTHORS / ЗАЯВЛЕННЫЙ ВКЛАД АВТОРОВ

The authors contributed equally to this article.

Все авторы внесли эквивалентный вклад в подготовку публикации.

8. CONFLICT OF INTERESTS / КОНФЛИКТ ИНТЕРЕСОВ

The authors have no conflicts of interest to declare. All authors have read and agreed to the published version of the manuscript.

Авторы заявляют об отсутствии у них конфликта интересов. Все авторы прочитали рукопись и согласны с опубликованной версией.

9. REFERENCES

Abdelsalam M.G., Stern R.J., 1996. Sutures and Shear Zones in the Arabian-Nubian Shield. Journal of African Earth Sciences 23 (3), 289–310. https://doi.org/10.1016/S0899-5362(97)00003-1.

Abdullah A., Nassr S., Ghaleeb A., 2013. Remote Sensing and Geographic Information System for Fault Segments Mapping a Study from Taiz Area, Yemen. Journal of Geological Research 2013, 1–16. http://dx.doi.org/10.1155/2013/201757.

Abuelnaga H.S., Aboulela H., El-Sawy E.K., El Qassas R.A.Y., 2019. Detection of Structural Setting that Controlling Hammam Faroun Area, Using Aeromagnetic and Seismicity Data, Gulf of Suez, Egypt. Journal of African Earth Sciences 158, 103560. https://doi.org/10.1016/j.jafrearsci.2019.103560.

Adiri Z., El Harti A., Jellouli A., Lhissou R., Maacha L., Azmi M., Zouhair M., Bachaoui E.M., 2017. Comparison of Landsat-8, ASTER and Sentinel 1 Satellite Remote Sensing Data in Automatic Lineaments Extraction: A Case Study of Sidi Flah-Bouskour Inlier, Moroccan Anti Atlas. Advances in Space Research 60 (11), 2355–2367. https://doi.org/10.1016/j.asr.2017.09.006.

Amer R., Kusky T., Ghulam A., 2010. Lithological Mapping in the Central Eastern Desert of Egypt Using ASTER Data. Journal of African Earth Sciences 56 (2–3), 75–82. https://doi.org/10.1016/j.jafrearsci.2009.06.004.

Awad H.A., El-Leil I.A., Nastavkin A.V., Tolba A., Kamel M., El-Wardany R.M., Rabie A., Ene A., Tekin H.O., Issa Sh.A.M., Zakaly H.M.H., 2022. Statistical Analysis on the Radiological Assessment and Geochemical Studies of Granite Rocks in the North of Um Taghir Area, Eastern Desert, Egypt. Open Chemistry 20 (1), 254–266. https://doi.org/10.1515/chem-2022-0131.

Boardman J.W., Kruse F.A., Green R.O., 1995. Mapping Target Signatures via Partial Unmixing of AVIRIS Data. In: Summaries of the Fifth Annual JPL Airborne Earth Science Workshop (January 23–26, 1995, Pasadena). Vol. 1. JPL Publication, p. 23–26.

Boulos F.K., Morgan P., Toppozada T.R., 1987. Microearthquake Studies in Egypt Carried Out by the Geological Survey of Egypt. Journal of Geodynamics 7 (3–4), 227–249. https://doi.org/10.1016/0264-3707(87)90008-1.

Casas A.M., Cortes A.L., Maestro A., Soriano M.A., Riaguas A., Bernal J., 2000. LINDENS: A Program for Lineament Length and Density Analysis. Computers & Geosciences 26 (9–10), 1011–1022. https://doi.org/10.1016/S0098-3004(00)00017-0.

Collins A.S., Pisarevsky S.A., 2005. Amalgamating Eastern Gondwana: The Evolution of the Circum-Indian Orogens. Earth-Science Reviews 71 (3–4), 229–270. https://doi.org/10.1016/j.earscirev.2005.02.004.

Colwell R.N., Estes J.E., Thorley G.A., 1983. Manual of Remote Sensing. Vol. 2: Interpretation and Applications. American Society of Photogrammetry, USA, 2440 p.

Dos Reis Salles R., de Souza Filho C.R., Cudahy T., Vicente L.E., Monteiro L.V.S., 2017. Hyperspectral Remote Sensing Applied to Uranium Exploration: A Case Study at the Mary Kathleen Metamorphic-Hydrothermal U-REE Deposit, NW, Queensland, Australia. Journal of Geochemical Exploration 179, 36–50. https://doi.org/10.1016/j.gexplo.2016.07.002.

Drury S.A., 1987. Image Interpretation in Geology. Kluwer Academic Publishers, p. 66–148.

Eldosouky A.M., 2019. Aeromagnetic Data for Mapping Geologic Contacts at Samr El-Qaa Area, North Eastern Desert, Egypt. Arabian Journal of Geosciences 12, 2. https://doi.org/10.1007/s12517-018-4182-2.

Eldosouky A.M., Mohamed H., 2021. Edge Detection of Aeromagnetic Data as Effective Tools for Structural Imaging at Shilman Area, South Eastern Desert, Egypt. Arabian Journal of Geosciences 14, 13. https://doi.org/10.1007/s12517-020-06251-4.

Eldosouky A.M., Saada A.S., 2020. Source Edge Detection (SED) of Aeromagnetic Data: Synthetic Examples and a Case Study from Haimur Area, South Eastern Desert, Egypt. Arabian Journal of Geosciences 13, 626. https://doi.org/10.1007/s12517-020-05653-8.

El-Gaby S., List F.K., Tehrani R., 1988. Geology, Evolution and Metallogenesis of the Pan-African Belt in Egypt. In: S. El-Gaby, R.O. Greiling (Eds), The Pan-African Belt of Northeast Africa and Adjacent Areas: Tectonic Evolution and Economic Aspects of a Late Proterozoic Orogen. Vieweg & Sohn, Braunschweig, Wiesbaden, p. 17–68.

El Kati I., Nakhcha C., El Bakhchouch O., Tabyaoui H., 2018. Application of Aster and Sentinel-2A Images for Geological Mapping in Arid Regions: The Safsafate Area in the Neogen Guercif Basin, Northern Morocco. International Journal of Advanced Remote Sensing and GIS 7 (1), 2782–2792. DOI:10.23953/cloud.ijarsg.374.

El-Leil I.A., Bekhit M.H., Tolba A.S., Moharem A.F., Shahin T.M., 2015. Geological, Structural and Petrotectonical Aspectable Features of Neoproterozoic Rocks, Gabal El Dob Area, Northeastern Desert, Egypt. International Journal of Scientific Engineering and Applied Science 1 (8), 332–350.

Farahbakhsh E., Chandra R., Olierook H.K.H., Scalzo R., Clark C., Reddy S.M., Müller R.D., 2018. Computer Vision-Based Framework for Extracting Geological Lineaments from Optical Remote Sensing Data. International Journal of Remote Sensing 41 (5), 1760–1787. https://doi.org/10.1080/01431161.2019.1674462.

Javhar A., Chen X., Bao A., Jamshed A., Yunus M., Jovid A., Latipa T., 2019. Comparison of Multi-Resolution Optical Landsat-8, Sentinel-2 and Radar Sentinel-1 Data for Automatic Lineament Extraction: A Case Study of Alichur Area, SE Pamir. Remote Sensing 11 (7), 778. https://doi.org/10.3390/rs11070778.

Johnson P.R., Andresen A., Collins A.S., Fowler A.R., Fritz H., Ghebreab W., Kusky T., Stern R.J., 2011. Late Cryogenian – Ediacaran History of the Arabian – Nubian Shield: A Review of Depositional, Plutonic, Structural, and Tectonic Events in the Closing Stages of the Northern East African Orogen. Journal of African Earth Sciences 61 (3), 167–232. https://doi.org/10.1016/j.jafrearsci.2011.07.003.

Kocal A., Duzgun H.S., Karpuz C., 2004. Discontinuity Mapping with Automatic Lineament Extraction from High Resolution Satellite Imagery. In: Geo-Imagery Bridging Continents. Proceedings of XX International Society for Photogrammetry and Remote Sensing Congress (July 12–23, 2004, Istanbul). Vol. XXXV. Part B7. ISPRS, p. 1073-1078.

Koike K., Nagano S., Ohmi M., 1995. Lineament Analysis of Satellite Images Using a Segment Tracing Algorithm (STA). Computers & Geosciences 21 (9), 1091–1104. https://doi.org/10.1016/0098-3004(95)00042-7.

Kröner A., Krüger J., Rashwan A.A.A., 1994. Age and Tectonic Setting of Granitoid Gneisses in the Eastern Desert of Egypt and South-West Sinai. Geologische Rundschau 83, 502–513. https://doi.org/10.1007/BF00194157.

Li P., Wu W., Wen Y., Zhang C., Zhang J., Zhang S., Yu Z., Yang S.A., Manchon A., Zhang X., 2018. Spin-Momentum Locking, and Spin-Orbit Torques in Magnetic Nano-Heterojunctions Composed of Weyl Semimetal WTe_2. Nature Communications 9, 3990. https://doi.org/10.1038/s41467-018-06518-1.

Liu L., Zhou J., Yin F., Feng M., Zhang B., 2014. The Reconnaissance of Mineral Resources through Aster Data-Based Image Processing, Interpreting and Ground Inspection in the Jiafushaersu Area, West Junggar, China. Journal of Earth Science 25, 397–406. https://doi.org/10.1007/s12583-014-0423-9.

Liu Z., Han L., Du Ch., Cao H., Guo J., Wang H., 2021. Fractal and Multifractal Characteristics of Lineaments in the Qianhe Graben and Its Tectonic Significance Using Remote Sensing Images. Remote Sensing 13 (4), 587. https://doi.org/10.3390/rs13040587.

Madani A.A., 2001. Selection of the Optimum Landsat Thematic Mapper Bands for Automatic Lineaments Extraction, Wadi Natash Area, South Eastern Desert, Egypt. Proceedings of the 22nd Asian Conference on Remote Sensing (November 5–9, 2001, Singapore). Avalable from: https://a-a-r-s.org/proceeding/ACRS2001/Papers/GEO-04.pdf (Last Accessed April 21, 2021).

Mandanici E., Bitelli G., 2016. Preliminary Comparison of Sentinel-2 and Landsat 8 Imagery for a Combined Use. Remote Sensing 8 (12), 1014. https://doi.org/10.3390/rs8121014.

Mars J.C., Rowan L.C., 2006. Regional Mapping of Phyllic- and Argillic-Altered Rocks in the Zagros Magmatic Arc, Iran, Using Advanced Spaceborne Thermal Emission and Reflection Radiometer (ASTER) Data and Logical Operator Algorithms. Geosphere 2 (3), 161–186. https://doi.org/10.1130/GES00044.1.

Morris K., 1991. Using Knowledge-Base Rules to Map the Three-Dimensional Nature of Geological Features. Photogrammetric Engineering & Remote Sensing 57 (9), 1209–1216.

Nair A., Mathew G., 2012. Lithological Discrimination of the Phenaimata Felsic–Mafic Complex, Gujarat, India, Using the Advanced Spaceborne Thermal Emission and Reflection Radiometer (ASTER). International Journal of Remote Sensing 33 (1), 198–219. https://doi.org/10.1080/01431161.2011.591441.

Ni C., Zhang S., Liu C., Yan Y., Li Y., 2016. Lineament Length and Density Analyses Based on the Segment Tracing Algorithm: A Case Study of the Gaosong Field in Gejiu Tin Mine, China. Mathematical Problems in Engineering, 5392453. https://doi.org/10.1155/2016/5392453.

Papadaki E.S., Mertikas S.P., Sarris A., 2011. Identification of Lineaments with Possible Structural Origin Using ASTER Images and DEM Derived Products in Western Crete, Greece. EARSeL eProceedings 1 (10), 9–26.

Pham L.T., Eldosouky A.M., Oksum E., Saada S.A., 2020. A New High Resolution Filter for Source Edge Detection of

Potential Data. Geocarto International. https://doi.org/10.1080/10106049.2020.1849414.

Pham L.T., Oksum E., Vu M.D., Vo Q.T., Le-Viet K.D., Eldosouky A.M., 2021. An Improved Approach for Detecting Ridge Locations to Interpret the Potential Field Data for More Accurate Structural Mapping: A Case Study from Vredefort Dome Area (South Africa). Journal of African Earth Sciences 175, 104099. https://doi.org/10.1016/j.jafrearsci.2020.104099.

Pirasteh S., Pradhan B., Safari H.O., Ramli M.F., 2013. Coupling of DEM and Remote-Sensing-Based Approaches for Semi-automated Detection of Regional Geostructural Features in Zagros Mountain, Iran. Arabian Journal of Geosciences 6, 91–99. https://doi.org/10.1007/s12517-011-0361-0.

Prasad A.D., Jain K., Gairola A., 2013. Mapping of Lineaments and Knowledge Base Preparation Using Geomatics Techniques for Part of the Godavari and Tapi Basins, India: A Case Study. International Journal of Computer Applications 70 (9), 39–47. http://dx.doi.org/10.5120/11994-7875.

Ramli M.F., Yusof N., Yusoff M.K., Juahir H., Shafri H.Z.M., 2010. Lineament Mapping and Its Application in Landslide Hazard Assessment: A Review. Bulletin of Engineering Geology and the Environment 69, 215–233. https://doi.org/10.1007/s10064-009-0255-5.

Sedrette S., Rebai N., 2016. Automatic Extraction of Lineaments from Landsat Etm+ Images and Their Structural Interpretation: Case Study in Nefza Region (North West of Tunisia). Journal of Research in Environmental and Earth Sciences 4, 139–145.

Sehsah H., Eldosouky A.M., 2020. Neoproterozoic Hybrid Forearc – MOR Ophiolite Belts in the Northern Arabian-Nubian Shield: No Evidence for Back-Arc Tectonic Setting, International Geology Review 64 (2), 151–163. https://doi.org/10.1080/00206814.2020.1836523.

Si Mhamdi H., Raji M., Maimouni S., Oukassou M., 2017. Fractures Network Mapping Using Remote Sensing in the Paleozoic Massif of Tichka (Western High Atlas, Morocco). Arabian Journal of Geosciences 10, 125. https://doi.org/10.1007/s12517-017-2912-5.

Singh A., Harrison A., 1985. Standardized Principal Components. International Journal of Remote Sensing 6 (6), 883–896. https://doi.org/10.1080/01431168508948511.

Soulaimani A., Admou H., Youbi N., Hafid A., Hefferan K.P., 2014. Application of ASTER Remote Sensing Data to Geological Mapping of Basement Domains in Arid Regions: A Case Study from the Central Anti-Atlas, Iguerda Inlier, Morocco. Arabian Journal of Geosciences 7, 2407–2422. https://doi.org/10.1007/s12517-013-0945-y.

Stern R.J., 1994. Arc Assembly and Continental Collision in the Neoproterozoic East African Orogen: Implications for the Consolidation of Gondwanaland. Annual Review of Earth and Planetary Sciences 22, 319–351. https://doi.org/10.1146/annurev.ea.22.050194.001535.

Sulaksana N., Helman A., 2014. The Analysis of Remote Sensing Imagery for Predicting Structural Geology in Berau Basin East Kalimantan. International Journal of Science and Research 3 (4), 18–21.

Vail J.R., 1983. Pan-African Crustal Accretion in North-East Africa. Journal of African Earth Sciences 1 (3–4), 285–294. https://doi.org/10.1016/S0731-7247(83)80013-5.

Valero S., Chanussot J., Benediktsson J.A., Talbot H., Waske B., 2010. Advanced Directional Mathematical Morphology for the Detection of the Road Network in Very High-Resolution Remote Sensing Images. Pattern Recognition Letters 31 (10), 1120–1127. https://doi.org/10.1016/j.patrec.2009.12.018.

Van der Meer F.D., van der Werff H.M.A., van Ruitenbeek F.J.A., 2014. Potential of ESA's Sentinel-2 for Geological Applications. Remote Sensing of Environment 148, 124–133. https://doi.org/10.1016/j.rse.2014.03.022.

Wang M., Howarth P.J., 1993. Modeling Errors in Remote Sensing Image Classification. Remote Sensing of Environment 45 (3), 261–271. https://doi.org/10.1016/0034-4257(93)90109-B.